Imaging Electrons in Few-Electron Quantum Dots

A thesis presented

by

Parisa Fallahi

to

The Division of Engineering and Applied Science
in partial fulfillment of the requirements
for the degree of
Doctor of Philosophy
in the subject of

Applied Physics

Harvard University
Cambridge, Massachusetts

June 2006

Thesis advisor

Robert M. Westervelt

Author

Parisa Fallahi

Imaging Electrons in Few-Electron Quantum Dots

Abstract

Electrons in a one-electron quantum dot were imaged in the Coulomb blockade regime at liquid He temperatures using a cooled scanning probe microscope (SPM). The SPM images are obtained by scanning a charged tip above the surface of the quantum dot and recording the conductance through the quantum dot in the Coulomb blockade regime as a function of tip position. The lowest energy level in the dot is shifted by the charged SPM tip. This creates a ring of high conductance in the SPM image corresponding to a Coulomb Blockade peak. Fits to the lineshape of the ring determine the tip-induced shift of the electron energy state in the dot.

A technique for extracting the amplitude of the electronic wavefunction inside a quantum dot using a scanning probe microscope was proposed. A map of the shift in the energy level inside the quantum dot as a function of tip position is calculated from the SPM images. This energy shift, in first order perturbation theory, is given by a convolution of the wavefunction inside the quantum dot and the SPM tip potential. The wavefunction can therefore be calculated using a deconvolution method. The requirements for utilizing this technique include having a sharp tip perturbation relative to the size of the dot, low noise in the conductance measurements and knowing the shape of the tip perturbation accurately.

We have imaged the last electron in a quantum dot in a strong perpendicular magnetic field. Images show a ring of high conductance between zero and one electrons that shrinks in size and changes shape as the magnetic field is increased. We demonstrate that change in the ring diameter is mainly due to the diamagnetic shift in the one-electron ground state energy level in the dot: we estimate the diamagnetic shift, independent of the images, assuming a non-interacting electron picture, and show that the shrinking of the Coulomb blockade ring is consistent with the estimated diamagnetic energy shift. The shrinking of the ring can therefore be used as a measure of the diamagnetic shift of electrons in a quantum dot.

Contents

Acknowledgments

During the past several years at Harvard my path has met with the paths of many wonderful people who have touched my life, supported me, and made me a better person and a better scientist, and to whom I owe immense gratitude.

My advisor Robert Westervelt has created a great atmosphere for research in his lab at Harvard. During the six years I spent at his lab he has always been available for discussions, full of new ideas, and supportive and understanding. I would like to thank Bob for his endless support and encouragement through every stage of my graduate work.

I would like to thank my PhD thesis committee members, Eric Heller and Michael Tinkham, for their continuous advice and help during my time at Harvard, for the many meetings and signatures on my progress reports, for their support during my search for a future research lab and most importantly for running outstanding research groups that I have greatly benefited from collaborating and working with.

Michael Stopa came to Harvard about two years ago and made a difference in the lives of many researchers Here. Mike is a brilliant scientist and teacher from whom I have learned a great deal. I would like to thank Mike for his support, friendship and encouragement.

Research in Bob's lab is a team effort and for me one of the great joys of research is working with the team. I have collaborated closely with a number of people in the Westervelt and Heller groups. I would like to thank them all for showing me, in their own ways, better research and team-work. Thank you Ian Chan, Andy Vidan, Ania Bleszynski, Jian Huang, Jamie Walls and Muhammed Yildirim.

I have overlapped with and got to know many other members of the Westervelt

group. In the past two years I have worked closely with Kathy Aidala, and found in her a great collaborator and a friend. I would like to thank Kathy for great conversations, the tea breaks at the square and a great taste in fine dining! I would like to thank Mark Topinka for being a mentor and a friend. I would like to thank Brian LeRoy for writing a great thesis and for answering many questions even from the Netherlands. I would like to thank Hak-Ho Lee for always having a smile, never looking frustrated and sharing his valuable experiences as a student a year ahead of me! I would like to thank Tom Hunt for his never ending optimism and his fresh look at any situation. I would like to thank David Issadore for reminding me that there are still physicists who care about the world! I have enjoyed working with the new students in lab, Erin Boyd, Melaku Muluneh and Halvar Trodahl, and wish them all the best!

The Tinkham group lived down the Hall from the Westervelt group for many years and was a valuable neighbor! I would like to thank Sergio Valenzuela, William Neils, Steve Cronin and John Free for their willingness to help, answer numerous questions, and for many fun conversations. I would like to thank the Marcus and the Capasso groups for being fun, cooperative and helpful neighbors.

My special thanks goes to Steve Shepard and Yuan Lu for their enthusiasm to hear about the different fabrication projects and their willingness to help with making them work. I would like to thank Naomi Brave who has been a pleasure to know and interact with and who has kept the group running smoothly in many respects. Ralph Generazzo does a fantastic job at running the purchasing department and I would like to thank him for always being ready to answer questions and clear confusions.

Its been great to stop by and say hi to Tomas Rosado and Matt Toomey in the stockroom, I would like to thank them both for their great work. I am specially grateful for Tomas's great flan recipe and amazing barbecues.

My friends at Harvard have been an invaluable part of my time here. I met Cindy Hancox, Shiyamala Thambyahpillai, Tanya Zelevinsky and Melissa Wessels in my first year and started a friendship that I hope will last for much longer than these 7 years. I like to thank them for many nights out, coffee breaks, birthday celebrations, and for always being there.

I have shared apartments in Cambridge with amazing roommates who became precious friends. I would like to thank Sarah Eltantawi, Kareem Eltantawi, Ore Somolu, Charlotte Szilagyi, Sergi Elizalde, Hazhir Rahmandad, Meenoo Chahbazi and Maryam Mirzakhani for many laughs, great dinners, brilliant discussions, rocking parties, and for making my life so much richer.

I consider myself extremely fortunate to have been involved with an amazing peer counseling group at Harvard: InCommon. I met an extraordinary group of people there many of whom became very good friends of mine. I would like to thank InCommon, my friends there, and specially Frank McNamara, the group advisor, from whom I have learned a great deal about life, caring for others, and about Harvard!

I like to thank my wonderful friends who throughout the years have been my family in Cambridge! Thank you Maryam Mirzakhani, Payman Kassaie, Roya Beheshti, Neda Beheshti, Chahriar Assad, Yue Nina Chen, Ghazal Gheshnizjani, Mathieu Le Corre, Mehdi Yahyanejad, Michelle Povinelli, Mehdi Alighanbari, Babak Amirparviz, Farzan Parsinejad, Sarah Passone, Hazhir Rahmandad, Sara Sarkhili, Mohammad

Hafezi, Salomeh Siavoshi, Adel Ahanin, Neda Farahbakhsh, Jahan Ramezani, Saveez Saffarian, Shanti Deemyad and many others.

I can not begin to thank my parents Azam Pourghazi and Taghi Fallahi who have supported me in every decision I have made and have been encouraging, loving, accepting and much more. Thank you Azamjoon and Baba! My Brother Behzad and his wife Saghi have been great friends, I would like to thank them for their love, energy and encouragement. I could not be here without the love and support of Hamid Pourghazi and Marjan Sadjadi. I would like to thank them for always being there for me like second parents. Farideh and Behrouz khankhanian are my family in the US, I like to thank them for their encouragement and love throughout my years in Boston. I would like to thank Saeed pourghazi for many long conversations, good advice, and being forever willing to listen! Last but not least I would like to thank my aunts, uncles, cousins and family who make my visits to Iran, London, and California heart-warming and memorable.

Finally I would like to thank Dominik Zumbuhl for being a wonderful friend, for being there in my rainy and sunny days, for his love and support, and for making me see myself in a different, better way.

Chapter 1

Introduction

The field of mesoscopic physics owes a big part of its success and development to small man-made devices called quantum dots. A quantum dot is a semiconductor structure that contains a fixed number of electrons. Advancements in the growth of semiconductor heterostructures and in nano-lithography have made it possible to laterally define quantum dots in a two-dimensional electron gas (2DEG) using metallic surface gates. Laterally defined quantum dots offer a great level of flexibility and control over the design and tunability of the metallic surface gates that form the quantum dot. Important properties such as the number of electrons on the dot, the coupling to the source and drain leads, the shape and the energetics of the quantum dot can all be adjusted and controlled with gate voltages. Transport measurements have revealed a wealth of information about quantum dots in the past and continue to do so today. To extract spatial information about electrons inside quantum dots we have used a scanning gate microscopy (SGM) technique that combines transport measurements with scanning probe microscopy (SPM) at cryogenic temperatures.

This thesis presents the first scanning gate microscopy images of one-electron laterally defined quantum dots with and without a magnetic field and explores possibilities for imaging the electronic wavefunction inside the quantum dots.

Background

Two dimensional electron gases (2DEG) Electrons confined to an interface between two semiconductors in a semiconductor heterostructure can form a two-dimensional electron gas (2DEG). Molecular beam epitaxy (MBE) has made it possible to grow layers of different semiconductor materials with sub-monolayer precision, allowing for design and engineering of the conduction band, E_C. In a heterostructure containing a 2DEG the energy bands are designed such that the conduction band dips below the Fermi energy at the interface between two semiconductors. Figure 1.1 shows the band diagram of a GaAs/AlGaAs heterostructure containing a 2DEG. Electrons are confined to the quantum well formed at the interface of GaAs and AlGaAs. The Fermi energy E_F is determined by the donor layer density and surface states, and is designed to lie in between the first and second energy levels in the quantum well. The electrons occupying the first energy level inside the quantum well are free to move in a plane parallel to the surface and form a 2DEG. The atomically smooth interface between two semiconductors, made possible by the MBE growth, and the distance between the donors and the electron gas makes it possible to grow 2DEG samples with very high mobility, up to $\sim$30 million $\mathrm{cm^2V^{-1}s^{-1}}$. The high-mobility 2DEGs were crucial in the discovery and the ongoing study of integer and fractional quantum Hall effect. Furthermore higher mobility corresponds to longer mean free

paths for electrons, allowing for the study of ballistic electrons in mesoscopic devices such as quantum dots.

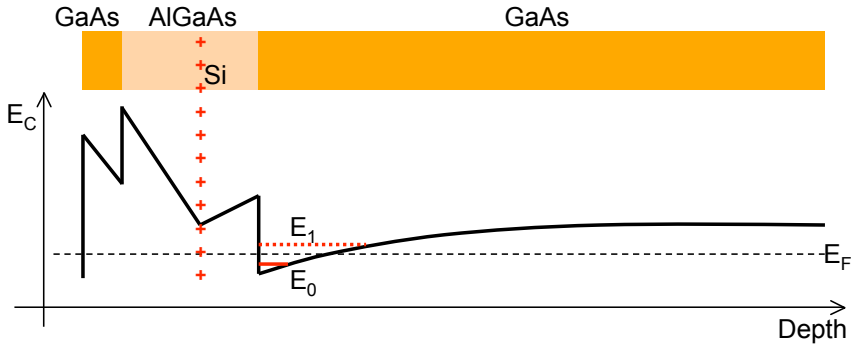

Figure 1.1: Conduction band of a GaAs/AlGaAs heterostructure containing a 2DEG plotted as a function of the depth below the surface. The offset between the conduction bands of GaAs/AlGaAs causes a discontinuity at the interface between GaAs and AlGaAs. The Electric field caused by the Si donors bends the conduction band and forms a quantum well at the interface. The conduction band dips below the Fermi energy E_F at the interface such that E_F lies between the first and second energy levels inside the quantum well. The electrons occupying the first energy level inside the quantum well form a 2DEG. The atomically smooth interface between GaAs and AlGaAs and the distance between the Si donor atoms and the electrons in the 2DEG makes it possible to form 2DEGs with very high mobility.

Laterally defined quantum dots Lateral quantum dots are formed by metallic gates patterned on the surface of a semiconductor heterostructure containing a 2DEG, using electron beam lithography techniques. Negative voltages applied to the surface gates deplete the electrons underneath and isolate a region of the 2DEG inside the quantum dot from the leads. The electrons in the isolated region of the 2DEG are confined in three dimensions. Figure 1.2 shows an example of a laterally defined quantum dot. The electrons inside the quantum dot are coupled to the source and drain leads through tunneling barriers formed between gates a and b and gates a and d, allowing transport measurements through the quantum dot to be performed. The

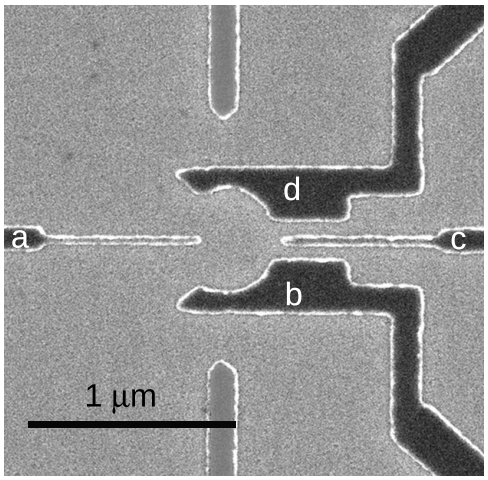

Figure 1.2: An SEM image of a lateral quantum dot formed using metallic surface gates in a GaAs/AlGaAs heterostructure containing a 2DEG. Gates a, b, c and d are used to form the quantum dot. Negative voltages applied to these gates deplete the 2DEG underneath and form a quantum dot by isolating a section of the 2DEG that lies within the gates from the leads. Tunneling barriers are formed between gates a and b and gates a and d. Gate c is often used to change the number of electrons on the quantum dot.

tunneling rates through these barriers can be changed by changing the gate voltages. The side gate c, also referred to as the plunger gate, couples strongly to the electrons in the quantum dot and weakly to the tunneling barriers. Gate c is often used to change the number of electrons on the dot without significantly affecting the tunneling rates.

Single-electron charging and Coulomb blockade Initial interest in quantum dots was sparked by single-electron charging effects or Coulomb blockade. Coulomb blockade results from the Coulomb repulsion of electrons on a quantum dot. The change in the chemical potential of the quantum dot as a result of adding an electron (the addition energy) is given by $E_C + \Delta$ (constant interaction model [1, 2]) where the charging energy $E_C = e^2/C$ (C = dot total capacitance) represents the Coulomb

interactions and Δ is the energy level spacing of the quantum states in the dot. In order to add an electron to the dot, sufficient energy must be supplied to overcome this charging energy, either through changing a gate voltage or applying a source to drain voltage V_{SD}. Electrons can therefore be added to the quantum dot one at a time, once one electron enters the dot further energy is needed to add another, leading to single-electron charging effects.

In order to experimentally observe single-electron charging effects, particular energy requirements must be met. Figure 1.3 shows a schematic of a quantum dot with the relevant energies. The tunnel barriers and the electrons in the leads are demonstrated by the dark and light orange areas respectively. Electrons in the leads have a Fermi distribution with a broadening around the Fermi energy E_F given by k_BT. The energy levels inside the quantum dot are filled if they lie below E_F and are empty otherwise. The addition energy $E_C + \Delta$ and the lifetime broadening of the energy levels inside the quantum dot $\hbar\Gamma$ (Γ is the tunneling rate through the barriers) are indicated. In order to observe single-electron charging we need $E_C > \hbar\Gamma$ and $E_C >> k_BT$. The relative values of k_BT, $\hbar\Gamma$ and Δ determine the line shape of a conductance peak [3].

Coulomb blockade in semiconductors was first observed by Scott-Thomas *et al.* in narrow wires [4] and has been widely studied since [3]. Transport measurements through quantum dots are mainly based on Coulomb blockade. In a plot of quantum dot conductance as a function of a gate voltage peaks are observed in the dot conductance every time an electron is added to the dot. The separation of these peaks is a direct measure of the addition energy $E_C + \Delta$, giving spectroscopical information

about the dot. The ability to turn the current on and off using a small change in the gate voltage gives quantum dots the name single-electron transistors [5].

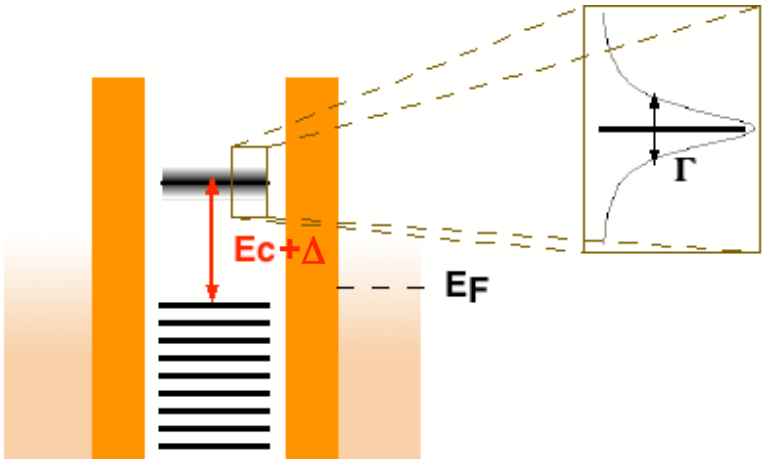

Figure 1.3: Schematic of a quantum dot. The tunnel barriers and the electrons in the leads are demonstrated by the dark and light orange areas respectively. The lowest empty energy level is separated from the last filled energy level by the addition energy $E_C + \Delta$. The lifetime broadening of the energy levels inside the dot is given by $\hbar\Gamma$ where Γ is the tunneling rate through the barriers. In order to observe single electron charging effects the charging energy E_C must be larger than both k_BT and $\hbar\Gamma$.

Design of few-electron quantum dots Quantum dots with only a few electrons were first made in the vertical dot geometry described in figure 1.5 [6]. Reaching the few electron regime in lateral quantum dots was a bigger challenge. The amplitude of a Coulomb blockade peak is determined by the tunneling rate through the tunnel barriers. If the two tunnel barriers are far from each other, once only few electrons are left in the quantum dot the coupling to one or the other of the tunnel barriers would be very small and the signal would be hard to measure. In vertical quantum dots the leads are above and below the quantum dot and the coupling of electrons to the leads is almost independent of the electron position, making it easier to reach few-electron

regimes. The first lateral quantum dot to hold only one electron was made by Ciorga *et al.* [7]. Figure 1.4a shows a micrograph of this lateral quantum dot in contrast to b that shows a more traditional quantum dot design. The main difference between the two designs is that in the Ciorga dot the two quantum point contacts are next to each other making it possible for even one electron to couple strongly to both tunnel barriers. The first one-electron quantum dot was followed by many other single and coupled one-electron lateral quantum dots [8, 9, 10, 11, 12] with similar designs.

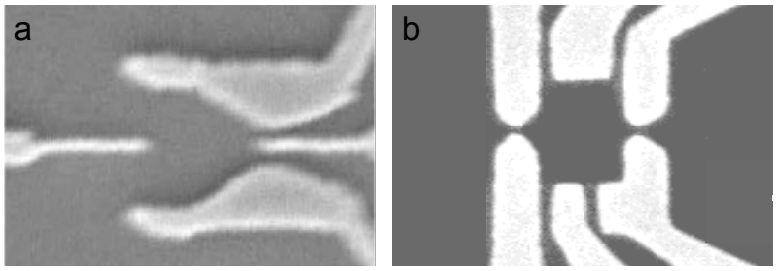

Figure 1.4: (a) Electron micrograph of the first lateral quantum dot to hold zero electrons [7]. The important feature of this design is having the two tunnel barriers next to each other, allowing a small number of electrons to couple strongly to both barriers. (b) A more traditional quantum dot design with tunnel barriers on opposite sides of the dot.

Quantum dots as artificial atoms One of the most fascinating aspects of quantum dots is their similarities to atoms that have given them the name artificial atoms [13, 14, 2]. Just as in real atoms, electrons in quantum dots are bound in a confining potential. If the quantum dot is sufficiently small discrete energy levels can be observed. This similarity was demonstrated in a beautiful experiment by Tarucha *et al.* [6, 2] in which transport measurements through a vertical quantum dot revealed shell filling and Hunds rule analogous to natural atoms. Figure 1.5a shows the schematic of the vertical quantum dot. The dot is formed in a quantum well between two AlGaAs

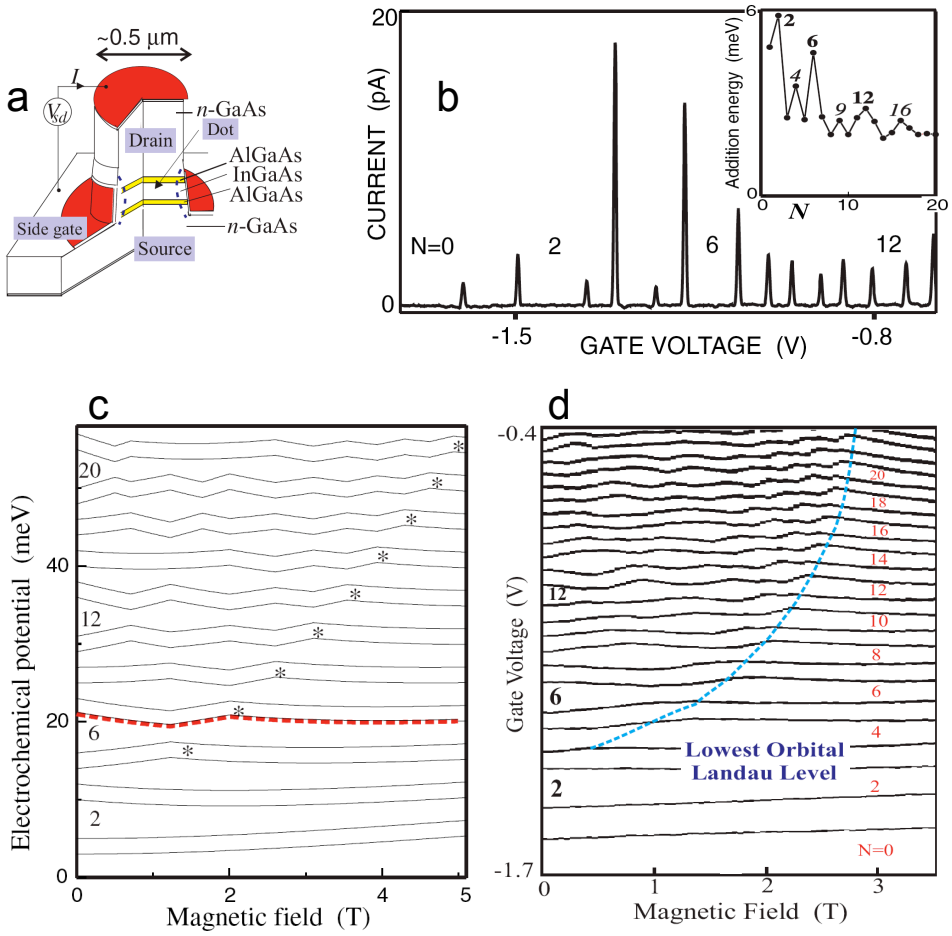

Figure 1.5: (a) Schematic diagram of a vertical quantum dot formed in an etched pillar in a GaAs/AlGaAs heterostructure. The AlGaAs layers act as tunneling barriers to the source and drain leads above and below the dot. (b) Plot of current through the quantum dot as a function of the side-gate volatge showing Coulomb blockade. The circular symmetry of the quantum dot leads to degeneracies in the energy states that form the shell structure. The spacing between the current peaks is proportional to the addition energy $E_C + \Delta$ where E_C is the charging energy and Δ is the level spacing. For degenerate levels the spacing between the peaks is only E_C while once a shell is filled the spacing increases to $E_C + \Delta$. The inset plots the peak spacing as a function of electron number, clearly demonstrating the shell filling effect. (c) Calculated evolution of the energy levels of a vertical quantum dot is a perpendicular magnetic field, given by the Fock-Darwin states [2]. (d) Measured current through the dot as a function of side-gate voltage and a perpendicular magnetic field. Great agreement with theory is observed.

tunneling barriers. The material around the quantum dot is etched away leaving a circularly symmetric pillar that provides the confinement in the direction parallel to the surface. This circular symmetry leads to degeneracies in the energy spectrum that form the shells. The spacing between the Coulomb blockade peaks shown in figure 1.5b reveals this shell structure as demonstrated in the inset.

Despite the similarities between quantum dots and real atoms the area of a quantum dot is significantly larger than that of an atom, by 3 to 4 orders of magnitude. The larger area makes quantum dots more sensitive to an applied magnetic field, opening up magnetic field regimes that are not accessible in real atoms. Figures 1.5 c and d show the predicted and measured behavior of the energy levels of the vertical quantum dot in a perpendicular magnetic field. The evolution of the energy levels with an increasing magnetic field reveals effects of magnetic confinement, and leads to ground state transitions already at a few Tesla. Such transitions would occur at magnetic fields of the order of 10^3 Tesla in real atoms, a regime not accessible in a laboratory.

Quantum dots as qubits A new wave of excitement and interest in lateral quantum dots came with ideas of quantum computing using a quantum dot. In a proposal by Loss and DiVincenzo an array of coupled lateral quantum dots was proposed as a building block for a quantum computer [15]. Figure 1.6 shows a schematic of this quantum dot array. Each quantum dot holds only one electron with the spin acting as a qubit. Lateral quantum dots are not the only candidates for qubits, any quantum mechanical two-level system with long enough coherence times and means to control the energy levels is a potential qubit. Other candidates for qubits include

trapped ions, linear optics, superconducting qubits, electrons on a liquid He surface and liquid state NMR. One of the advantages of lateral quantum dots over some of the other candidates is scalability, benefiting greatly from the advancements of the semiconductor industry in nano-fabrication. One of the limitations of lateral quantum dot spin qubits is strong interactions with the surrounding environment that leads to relatively shorter coherence times. Studies of coherence in quantum dots [16, 17, 18] have revealed spin relaxation time of the order of $T_1 = 100$ ms and spin decoherence times of the order $T_2 = 10$ ns. These studies show that the T_2 time can particularly suffer from interactions with nuclear spins. Understanding the underlying decoherence mechanisms and how to coherently control the states in a quantum dot spin qubit remains one of the main challenges in the study of lateral quantum dots.

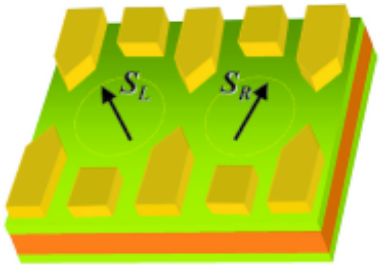

Figure 1.6: Schematic of the quantum dot array in the Loss-diVincenzo quantum computing proposal. Each electron in the array contains only one electron, the spin of which acts as the qubit. Adjacent quantum dots are tunnel coupled and the coupling can be adjusted using the gate voltages.

Scanning Probe Microscopy Scanning probe microscopy (SPM) is a technique that allows direct probing of spatial properties of a system at sub-micron length scales. Since its development in the early 1980s, and together with advances in nano-fabrication, SPM has opened up a wide range of opportunities in the study of small

sytems. In 1982 Binnig and Roher invented the scanning tunneling microscope (STM) and imaged atoms on the surface of a Si crystal for the first time [19]. This was soon followed by the invention of the atomic force microscope (AFM) in 1986[20]. These early scanning probe techniques lead the way to the development of a wide variety of imaging techniques that today form the field of scanning probe microscopy. Different SPM techniques are applicable to different systems and measure different properties. The basis of all SPM techniques is a very fine tip that is scanned above the system, while the differences lie in the feedback mechanism and the properties they measure. STM is applied to conductive samples and produces high-resolution topographical images as well as maps of local density of states. AFM, the most commonly used SPM, measures the topography of surfaces and is applicable to a wide range of materials including biological systems. Near-field optical microscopy (NSOM), magnetic force microscopy (MFM), electrostatic force microscopy (EFM), etc. are among the many examples of SPM techniques available today.

Scanning gate microscopy (SGM) is an SPM technique used to probe electrons in semiconductor heterostructures and various other mesoscopic devices. SGM involves scanning a charged conductive tip above the surface and measuring the conductance through the sample as a function of tip position. In contrast to other SPM techniques where the tip is used as a sensor, for example for measuring force in AFM or the tunneling current in STM, in SGM the tip is electrostatically perturbing the sample while conductance through the sample is measured. The tip in other words is acting as a movable gate that capacitively couples to the electrons. The great advantage of SGM over other SPM techniques that are used to probe electrons is that SGM

can image electrons that are buried underneath surfaces, for example electrons in a 2DEG, as long as screening effects of the layers in between the tip and the electrons are minimal. Great successes of SGM [21] include imaging coherent electron flow in a 2DEG [22, 23] and imaging electrons in the quantum Hall regime [24, 25, 26, 27, 28]. The work presented in this thesis applies SGM to lateral quantum dots formed in GaAs/AlGaAs heterostructures in the few-electron regimes and proposes a technique to extract the electron wavefunction from the SGM images.

Chapter 2

Experimental Techniques

The experiments described in this thesis involve low-temperature scanning probe microscopy of electrons in quantum dot devices built in GaAs/AlGaAs heterostructures. The following are four major steps involved in carrying out these experiments: (1) design and fabrication of the quantum dot device, (2) cooling down the device to liquid-He temperatures, (3) tuning the quantum dot device and (4) scanning probe combined with low-noise transport measurements. The Westervelt lab has a long history and much experience in all the above which has resulted in great fabrication recipes and low-temperature/low-noise techniques that work. Detailed description of these techniques and recipes can be found in the theses written by previous graduate students [29, 30, 31]. In this chapter I give a general description of the experimental techniques with more emphasis on newer additions.

2.1 Device fabrication

The quantum dot devices are built in GaAs/AlGaAs heterostructures grown using molecular beam epitaxy (MBE). These heterostructures are provided for us by our collaborators in Santa Barbara. The first step in preparing the device is to cleave the original wafer that contains the 2DEG into small chips on which the device will be fabricated. The chip must be large enough to contain all the features necessary for the device, including the large bonding pads, and must be small enough to fit on the sample holder of the measurement system; The new SPM in particular has a limited area where the chip can be mounted. Once cut to the right size the chips are cleaned in boiling TCE (Trichloroethylene), acetone and methanol. TCE removes grease and organic junk on the chip. The chips are dipped into methanol immediately following acetone to avoid leaving a residue on the chip when the acetone evaporates. Ultra-high purity N gas is used to blow dry the chips. It is important that the chips are cleaned carefully to avoid problems such as bad lift-off, bad metallization and the malfunctioning of the ohmic contacts or the device.

E-Beam lithography is used to pattern metal gates, ohmic contacts and etched mesas on the chip. Figure 2.1 shows the basic steps in patterning a metallic gate or an etched trench using e-beam lithography. An e-beam resisit, usually PMMA, is spun on the sample. The patterned areas are then exposed using a narrowly focused e-beam. Developing leaves a mask-like layer of resist on the surface. To fabricate a metallic gate the desired metal is then evaporated on the surface. In the last step the resist is dissolved and lifted off leaving a metallic pattern on the surface. Etched trenches are fabricated by placing the sample with the resist mask in an etching

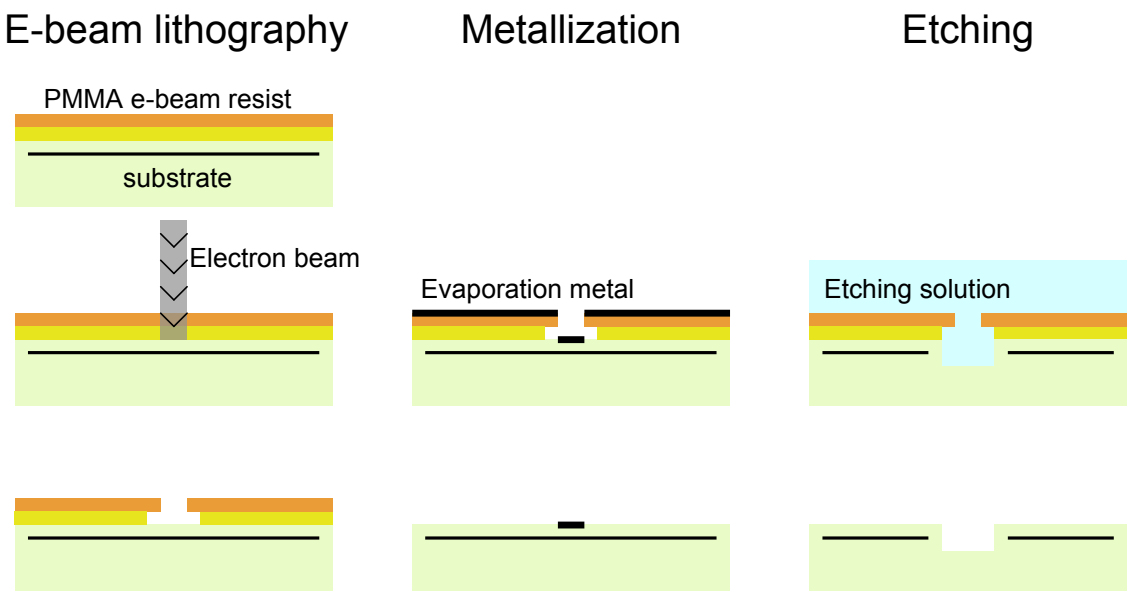

Figure 2.1: E-beam lithography steps in fabricating a metallic gate or an etched trench. The chip is covered with one or more layers of e-beam resist (PMMA) and exposed with a focused electron beam. Lift-off takes away the exposed areas of the resist, leaving a mask behind. To fabricate metallic gates a layer of the desired metal is evaporated on the sample. Dissolving the remaining resist leave only a metallic gate behind. In order to make etched trenches the sample with the resist mask is placed in an etching solution for a controlled time. Once the desired etching is achieved the etch is quenched and the resist removed.

solution for a controlled amount of time. The etching solution etches through the substrate and the 2DEG if necessary.

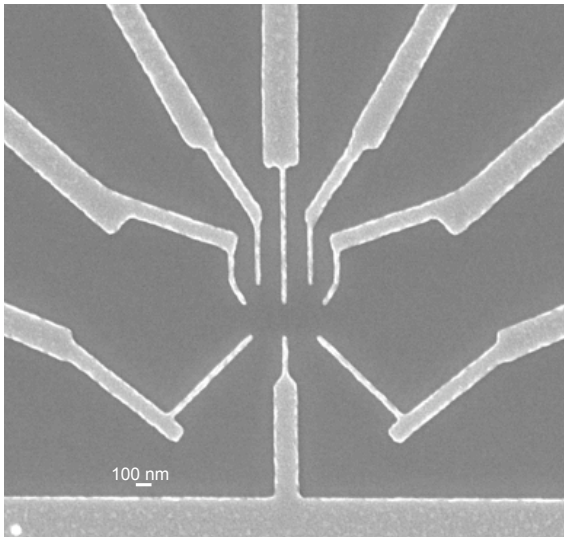

Figure 2.2: SEM micrograph of a double-dot device fabricated using e-beam lithography. A single layer of 950K PMMA was used. The thin gates were designed as single lines while the thicker gates were designed as rectangular areas. 10nm of Ti was evaporated to form the gates.

Choosing the right resist and spin conditions is key to fabricating a device successfully. PMMA (polymethyl methacrylate) is a commonly used high resolution e-beam resist. The company Michrochem produces PMMA in either 950,000 or 450,000 molecular weights resins in either chlorobenzene or anisole. The thickness of a PMMA layer spun on the surface of the chip is determined by the molecular weight, the solvent and the spin speed and time (see the PMMA data sheet available on Microchem websites for details). The optimal thickness for the PMMA layer depends on the desired pattern. When writing large patterns such as ohmic contacts or large gates a double or a triple layer of PMMA is recommended with the heavy layers on top. This provides an undercut, as shown on figure 2.1, that assists with the lift-off. Ohmic contacts and

larger gates also require a relatively thicker metallic layer, which necessitates a thicker PMMA layer. When writing small features using a thick PMMA layer reduces the resolution. The electron beam size in the e-beam machines available to us is smaller than 10 nm, however writing features smaller than 30nm is very challenging. This is due to the reduction in resolution caused by the thickness of the PMMA layer. Therefore for small features, if a thin metal layer is sufficient, using a single PMMA layer is recommended. Note that a small undercut is generated when using a single PMMA layer due to the backscattering of electrons from the surface and further exposing the PMMA closest to the surface of the sample.

The next set of parameters that need to be chosen carefully for writing small features are the exposure parameters. The combination of exposure dosage, dwell time, and step size determine how long the beam exposes a particular area of the pattern. To find the optimal exposure parameters it is strongly advised to write an exposure matrix, where the small features are written for a large range of exposure dosages that cover both the overexposed and underexposed limits. The dosages in between the two limits are the optimal values at which the writing process is least sensitive to dosage fluctuations due to bad focusing or current fluctuations. The exposure matrix could be repeated for different step sizes to find the optimal step size. Note that the exposure matrix needs to be repeated if the pattern is significantly changed, due to changes in the proximity effects.

Figure 2.2 shows an example of a device fabricated with small features. The thinner lines are single lines in the design while the rest of the gates are designed as rectangles. The optimal exposure parameters might be different for single lines

compared to areas. For this device a single layer of 950K PMMA was used . The gates are formed by evaporating 10 nm of Ti.

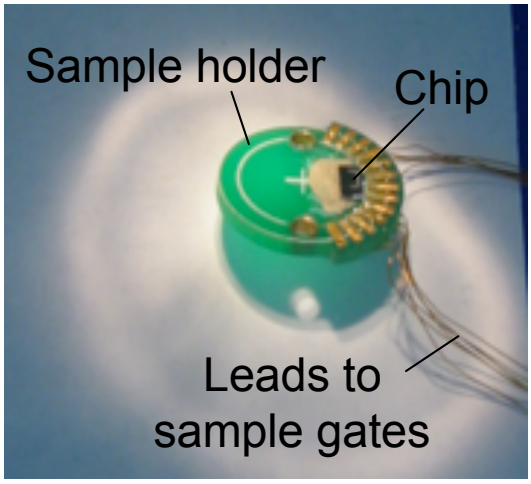

Figure 2.3: Devices mounted on the sample holder and wire-bonded. The GaAs chip, metallic pads on the chip and the gold-plated pads on the sample holder are seen. Silver paint was used to glue the sample to the sample holder.

Once the sample is ready, it is mounted on a sample holder and wire-bonded. This is shown in figure 2.3. The sample holder is then mounted on the microscope and cooled down to 1.7K. Cooling is done in three stages: cooling with liquid Ni to 77K, cooling with liquid He-4 to 4K, pumping on liquid He to lower the temperature to 1.7K. For temperatures below 4K the vapor pressure of the He-4 can be used as a direct measure of temperature.

2.2 Scanning probe measurements

Two different SPM microscopes were used for the work presented in this thesis. The images presented in chapter 3 were obtained in the He-4 microscope [29] and the images of chapter 5 were obtained using the He-3 microscope [30]. The operation

mechanisms of the two microscopes are very similar and is fully described in previous theses [29, 30]. In the following paragraphs I briefly describe how the microscopes work and their differences.

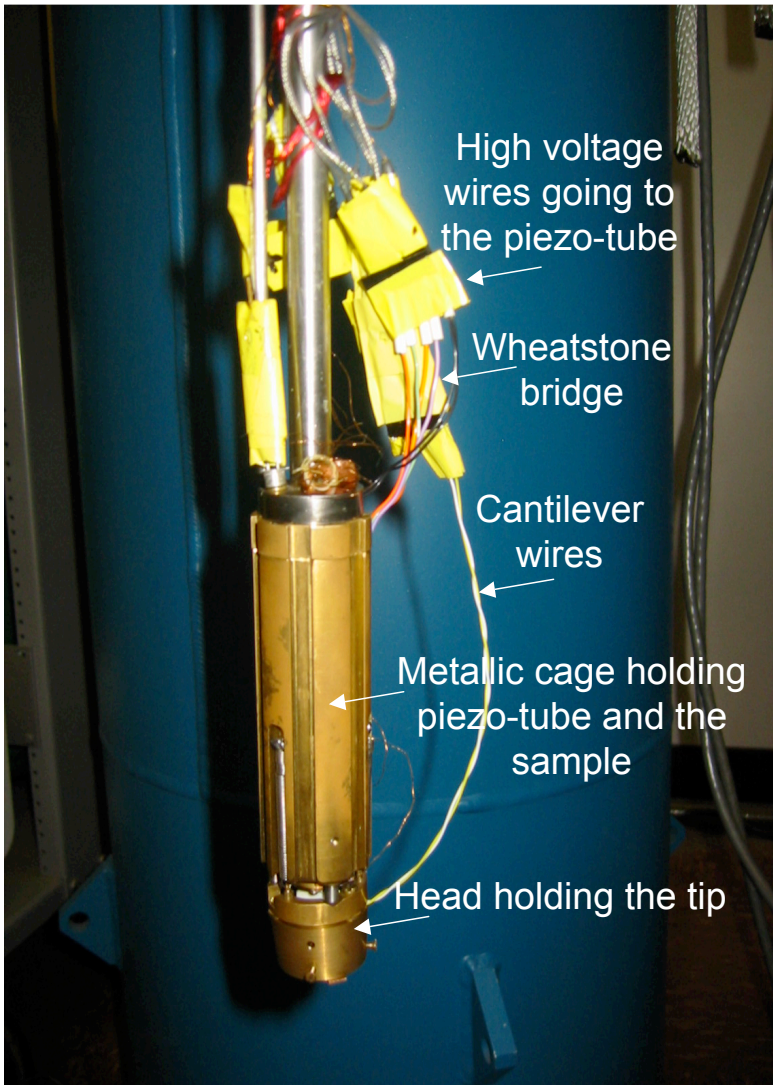

Figure 2.4: Picture of the microscope hanging upside down at the end of the insert. The bottom part holds the tip and the larger cage holds the piezo-tube and the sample.

Figure 2.4 shows the He-3 microscope as it hangs upside down at the bottom of the insert. There are two separate parts to the microscope held together using

springs. The head, sitting at the bottom in figure 2.4, holds the tip. The larger part holds a piezo-tube and the sample. The sample sits on top of the piezo-tube and is scanned underneath the tip. The microscope can be used to take topographical images of the sample surface as well as electrical scans. In the latter the tip is charged and scanned at a fixed height above the surface while the conductance through the sample is measured as a function of tip position. In our experiments topographical images are used to locate the quantum dot on the chip and to find the surface. Once the surface is found the tip height above the surface is set and conductance images can be obtained.

The position of the tip is controlled from a computer that is connected to a digital to analogue converter (DAC) with an optical cable. Figure 2.5 shows a schematic of the microscope electronics. The lines that carry the x and y voltages are shown in red. The DAC puts out a voltage between -10 and +10 Volts corresponding to positions in x or y of -10 to 10 microns at room temperature. To bend the piezo-tube in x or y, equal and opposite voltages should be applied to two opposite quadrants on the tube in the corresponding direction. The x and y voltages are therefore fed into a splitter/inverter box with four outputs, $\pm$x and $\pm$y. These voltages are then amplified 20 times and applied to the piezo tube.

The feed-back mechanism for the topographical image is based on the cantilever deflection. The SPM tip sits on a piezo-resistive cantilever that changes resistance upon deflection. Cantilever deflection can therefore be measured by measuring resistance of the cantilever. The cantilever signal measurement scheme is shown in figure 2.5 at the top of the page. The cantilever is part of a Wheatstone bridge that is

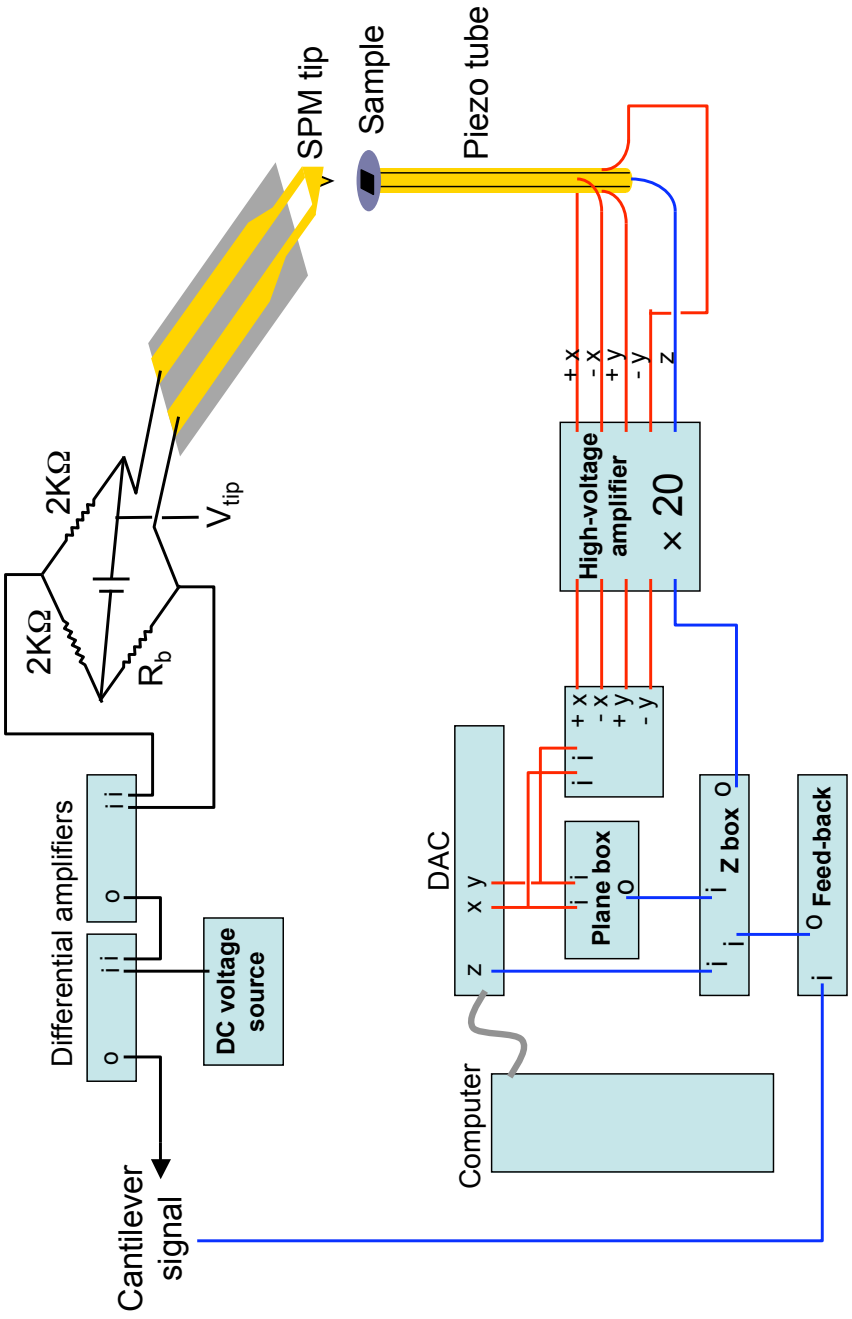

Figure 2.5: Schematic of the SPM electronics. The top part demonstrates the measurement of the cantilever signal. The bottom part shows how the scanning in x and y and the movements in z are achieved. The wires in red carry the x and y voltages to the piezo-tube while the lines in blue carry the z voltage.

placed right next to the microscope at liquid He temperature. Two 2K resistors and a balance resistor R_b form the other three arms of the bridge. The balance resistor is matched to the resistance of the (unbent) cantilever at room temperature. The voltage across the bridge is a measure of the cantilever resistance, and after 100,000 times amplification forms the cantilever signal.

The movement of the piezo-tube in the z-direction, i.e. perpendicular to the sample plane, can be controlled through a combination of three different voltages that are the inputs to the Z-box in figure 2.5. The Z-box outputs a sum of these three voltages which is applied to the piezo-tube after amplification. The first voltage is set by the computer and is output by the DAC, in the same way that x and y voltages are set. By changing the z-voltage on the computer the tip can be brought closer or further from the surface. The second voltage is the output of the plane-box. It is dependent on x and y and is set such that the tube follows the plane $z = ax + by$, where a and b are set by two knobs on the plane-box. The third voltage, used only for topographical imaging, is put out by the feedback box and is based on the cantilever signal. When taking a topographical image the tip is scanned while it is in contact with the surface and the cantilever deflects up or down as it goes over bumps and valleys of the surface. The deflection causes the cantilever signal to change to either more negative or more positive. The feedback box outputs a z-voltage that follows these changes, moving the piezo-tube away from the surface when the cantilever is bent too much and moving it the opposite direction when the cantilever is not bent enough, hence keeping the cantilever bent a fixed amount throughout the scan. The output of the feedback box can be used to form topographical images of the surface.

Conductance images are obtained by measuring the conductance through the device as a function of tip position. Here the tip is scanned at a fixed height above the surface and is negatively or positively charged. For these images the feedback box is off, the computer voltage is used to set the tip height above the surface and the plane-box is used to assure the tip height remains the same during the entire scan. For more sensitive scans, where the tip is brought very close to the surface and small changes in the tip to surface distance affects the images significantly, the SPM software is used to adjust the computer z-output such that it follows the surface of the sample. The plane that the software follows is determined by finding three different points on the surface close to the scanning area and fitting a plane to it.

The He-3 microscope is equipped with a 7T magnet, which was used in the experiment described in chapter 5. In this system the microscope sits in liquid He in contrast to the He-4 microscope that sits in vacuum. When the microscope is operated in liquid He the length of the operation time is limited, since the microscope can not be operated in He vapor due to voltage break downs between quadrants of the piezo-tube.

The conductance through the device is measured using standard lock-in techniques. Extra channels on the DAC are used to control the voltages on the gates or to supply a source to drain voltage. All the leads going to the sample gates are filtered and protected with a diode against going to positive voltages. Tuning a quantum dot in the Coulomb blockade regime can be a lengthy process that grows in difficulty with the number of additional gates on a dot. The entire gate parameter space needs to be explored to find the gate voltages that give the desired Coulomb blockade peaks

with the best signal to noise ratio. Once the dot is tuned, the Coulomb blockade peaks can be used to measure the temperature of the electrons. In the right regime the Coulomb blockade peaks are temperature broadened and their width is a direct measure of the thermal broadening of the electrons in the 2DEG.

Chapter 3

Imaging a one-electron quantum dot

3.1 Introduction

A scanning probe microscope (SPM) has proven to be a powerful tool to study, image, and manipulate mesoscopic systems. Electron waves in an open two-dimensional electron gas (2DEG) inside a semiconductor heterostructure were imaged using a liquid-He cooled SPM [21, 22, 23, 32]. In the quantum Hall regime, edge states and localized states were seen[24, 25, 26, 27, 28]. Furthermore an SPM was used to study electrons confined in nanostructures; charge oscillations due to the Coulomb blockade in quantum dots formed in a carbon nanotube were observed [33]. Imaging a single electron spin has been accomplished recently using a magnetic resonance force microscope (MRFM), where the signal from a single electron's spin resonance (ESR) was detected [34]. Molecule cascades arranged on a clean surface in ultrahigh vacuum by

a scanning tunneling microscope (STM) were used to perform logic operations [35].

Single-electron quantum dots are promising candidates for quantum information processing. The electron spin in each dot acts as a qubit, and tunneling is used to entangle spins on adjacent dots [15]. To pursue these ideas, quantum dots that contain only one electron are being developed, as individual single-electron dots [2, 6, 14, 7, 9] and as tunnel-coupled single-electron dots [8, 10]. A useful circuit for quantum information processing will consist of many coupled quantum dots. Scanning probe microscopy promises to be important for the development and understanding of quantum dots and dot circuits, by providing ways to image electrons and to probe individual dots using electromagnetic fields.

In this chapter we show how a liquid-He cooled scanning probe microscope with a charged tip can image a single-electron quantum dot in the Coulomb blockade regime. The dot was formed in a GaAs/AlGaAs heterostructure by surface gates. The charged tip shifts the lowest energy level in the dot and creates a ring in the image corresponding to a peak in the Coulomb-blockade conductance. Fits to the lineshape of the ring determine the tip-induced shift of the electron energy state in the dot.

3.2 Experimental Setup

The SPM imaging technique used to image the quantum dot is illustrated in figure 3.1. A charged SPM tip scanned above the surface can change the induced charge in a quantum dot (Figure 3.1b) and change the number of electrons. An image is obtained by recording the dot conductance G as the tip is scanned across

the sample. The voltage V_{tip} applied between the tip and the 2DEG perturbs the "bathtub" potential that holds electrons in the dot (Figure 3.1c). When the distance between the tip and the 2DEG is greater than the width of the wavefunction, as it was for the images in this paper, V_{tip} moves the bathtub up and down without changing the wavefunction's shape significantly, in a manner similar to the side-gate voltage V_G. When the tip is sufficiently close to the dot, closer than the width of the wavefunction, the tip voltage V_{tip} can change the shape of the wavefunction and thus the energy of the electron state above the bottom of the bathtub. The total shift ΔE in the ground state energy from both processes, indicated in Figure 3.1c, moves the gate-voltage position of the Coulomb-blockade conductance peak.

The quantum dot (Figure 3.1b) was formed in a GaAs/$Al_{0.3}Ga_{0.7}As$ heterostructure by Cr surface gates. The heterostructure contains a 2DEG 52nm below the surface, with measured density 3.8×10^{11} cm^{-2} and mobility 470,000 cm^2 V^{-1} s^{-1} at 4.2 K. The heterostructure was grown by molecular beam epitaxy with the following layers: 5 nm GaAs cap layer, 25 nm $Al_{0.3}Ga_{0.7}As$, Si delta-doping layer, 22 nm $Al_{0.3}Ga_{0.7}As$, 20 nm GaAs, 100 nm $Al_{0.3}Ga_{0.7}As$, a 200 period GaAs/$Al_{0.3}Ga_{0.7}As$ superlattice, 300 nm GaAs buffer and a semi-insulating GaAs substrate. The 2DEG is formed in a 20 nm wide GaAs square well between two $Al_{0.3}Ga_{0.7}As$ barriers. The sample was mounted in a liquid-He cooled SPM [22, 23] and cooled to T = 1.7 K.

Without the tip present, the quantum dot could be tuned to contain 0 or 1 electrons in the Coulomb blockade regime. This is clearly shown in Figure 3.2a, which plots the differential dot conductance dI/dV_{SD} vs. source-to-drain voltage V_{SD} and side gate voltage V_G at T = 1.7 K. The conductance peaks correspond to resonant

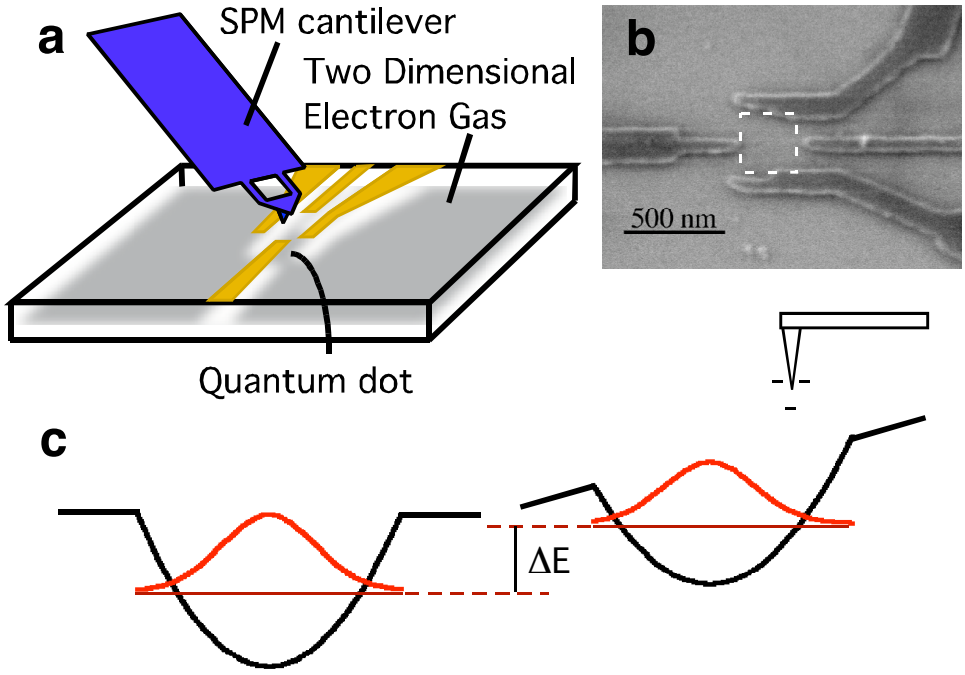

Figure 3.1: (a) Schematic diagram of the experimental set-up used to image electrons in a single-electron quantum dot. A charged scanning probe microscope (SPM) tip is scanned at a fixed height above the surface of the GaAs/AlGaAs heterostructure containing the dot. Images are obtained by recording the Coulomb blockade conductance G vs. tip position. (b) A scanning electron micrograph of the quantum dot. The dashed line indicates the area covered by the conductance images. (c) Schematic diagram that shows how the potential holding an electron in the dot is affected by the charged tip. The tip-induced shift ΔE in the energy of the electron state changes the Coulomb blockade conductance of the dot.

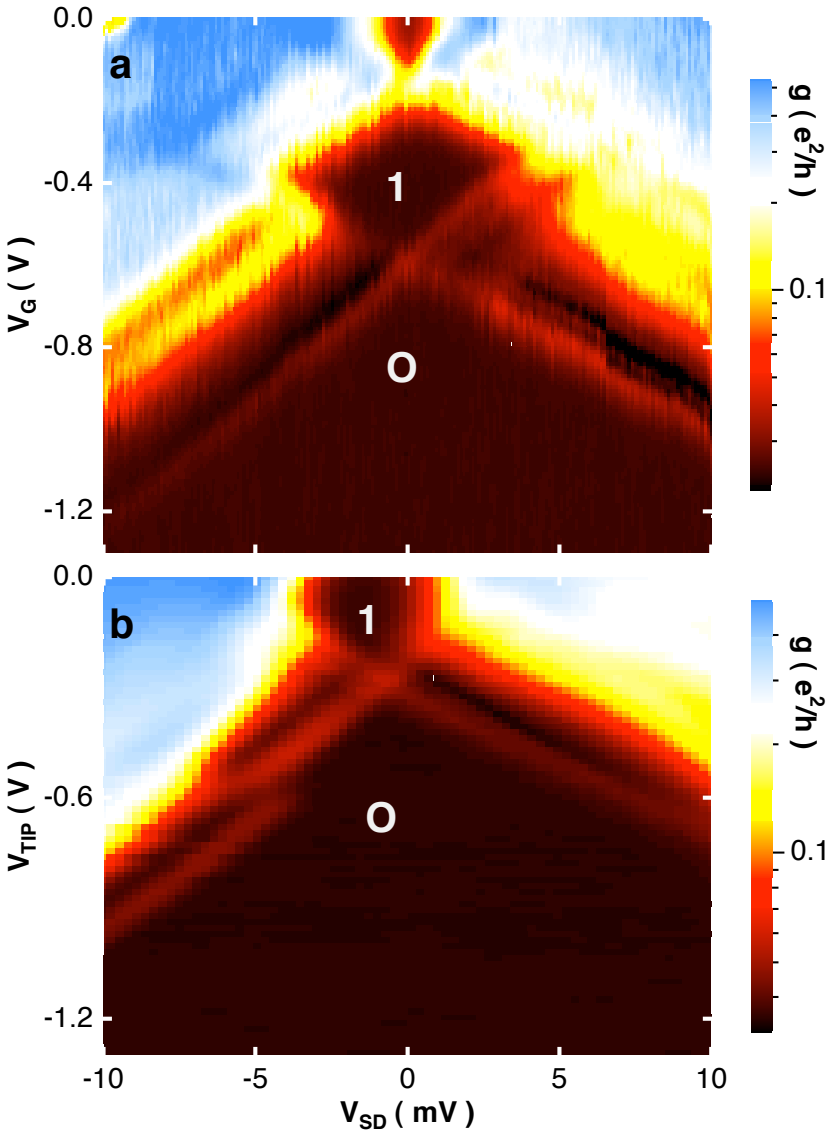

Figure 3.2: (a) Plot of differential conductance $g = dI/dV_{SD}$ as a function of side-gate voltage V_G and source-to-drain voltage V_{SD} at T = 1.7 K, showing Coulomb blockade diamonds for 0 and 1 electrons, and resonant tunneling through the ground and first excited energy levels separated by 3.1 meV. (b) Plot of differential conductance $g = dI/dV_{SD}$ vs. SPM tip voltage V_{tip} and V_{SD} at T = 1.7 K for a fixed tip position, showing that the tip acts as a moveable gate.

tunneling through a single quantum state. Coulomb blockade diamond measurements reveal an appreciable amount of information: from Figure 3.2a we determine the one-electron charging energy 4.2 meV and the ground-state to first-excited-state energy spacing 3.1 meV.

Figure 3.2b shows the differential conductance $g = dI/dV_{SD}$ vs. source-to-drain voltage V_{SD} for fixed V_G; here the tip voltage V_{tip} is used to change the induced charge on the dot with the tip held at a fixed position near the dot. The pattern of Coulomb blockade diamonds is similar to those obtained by varying V_G in Figure 3.2a, demonstrating that the tip acts as a gate, and that the tip to dot coupling is similar to the coupling between the side-gate and the dot. Because the tip can be arbitrarily positioned over the sample, it can be used as a movable gate to change the number of electrons on a quantum dot, as well as to direct electrons in a desired direction. These abilities promise to be very useful for the development of quantum dot circuits for quantum information processing.

3.3 Experimental Results

Images of the single-electron quantum dot were obtained at T = 1.7 K by recording the Coulomb blockade conductance with V_{tip} and V_G fixed, and $V_{SD} = 0$ V, while the tip was spatially scanned over the quantum dot, 100 nm above the surface. A series of images are shown in Figures 3.3a-d for tip voltages 40mV, 50mV, 60mV and 80mV respectively. The field of view covers an area within the gates of the quantum dot (see Figure 3.1b). In each image, a ring-shaped feature is observed, centered on the middle of the dot. The ring represents a contour of constant tip to dot coupling at

which the Coulomb blockade conductance is on a peak. This peak corresponds to resonant tunneling through the lowest energy level of the dot. The dot contains one electron when the tip is outside the ring and zero electrons when the tip is inside the ring. To confirm that the dot is empty inside the ring, we moved V_G to more-negative voltages and verified that no additional conductance peaks appeared.

The strength of the interaction between the SPM tip and the dot can be adjusted by changing the tip voltage V_{tip} as shown in Figures 3.3a-d. In Figure 3.3a the tip pushes the electron off the dot when the tip is about 100 nm to the side of the center. As V_{tip} is increased in a series of steps from Figures 3.3a to 3.3d, the radius of the ring shrinks to a small value. As discussed below, the lineshape of the ring provides a window through which one can extract information about the dot. The probing window can be moved to any desired location with respect to the dot by changing the ring radius.

The spatial resolution in Figures 3.3a-d is quite good, finer than the width of the tip electrostatic potential $\Phi_{tip}(\vec{r}, \vec{r}_{tip})$ at the point $\vec{r}$ in the 2DEG for tip position $\vec{r}_{tip}$; this width is determined in part by the height of the tip above the surface. The resolution is enhanced by the strong dependence of the Coulomb blockade conductance G on the change ΔE in electron energy. However, the images in Figure 3.3 do not determine the shape of wavefunction amplitude $|\psi(\vec{r})|^2$, because it is much narrower than $\Phi_{tip}(\vec{r}, \vec{r}_{tip})$ for this case.

Simulated images of the single-electron quantum dot are shown in Figures 3.3e-h. These images show the calculated dot conductance as a function of lateral tip position using parameters from the experiment, including the tip voltage and height. In these

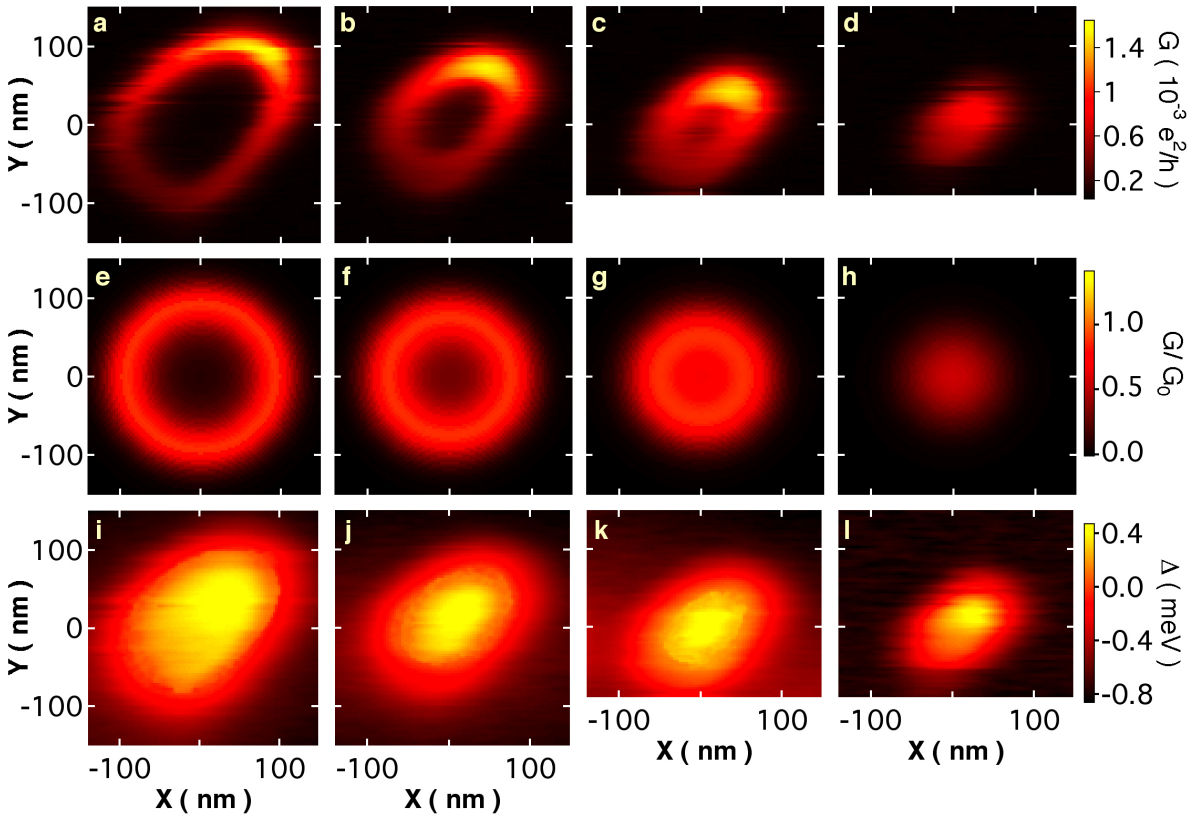

Figure 3.3: (a-d) Coulomb blockade images of a single-electron quantum dot at T = 1.7 K, showing the dot conductance G vs. tip position. The ring of high conductance around the center of the dot is formed by the Coulomb blockade peak between 0 and 1 electron in the dot. The tip voltages V_{tip} for a-d are 40 mV, 50 mV, 60 mV and 80 mV respectively. (e-h) Theoretical simulations of the images in a-d for a dot formed by a parabolic potential with energy spacing 3.1 meV (energy of first excited state from Figure 3.2a) for the same tip voltages as a-d. (i-l) Experimental maps of the energy shift Δ_{E_F} of electrons in the dot vs. tip position, extracted from the measured lineshape of the Coulomb blockade conductance peak forming the rings in images a-d.

calculations the dot was assumed to have a parabolic confining potential with an energy level spacing of 3.1 meV matching the measured value for the first excited state from Figure 3.2a. The ground state energy of the dot in the presence of the tip was obtained by solving Schrödingers equation for this system. The dot conductance was calculated in the resonant tunneling regime, involving only a single energy level in the dot [3]. The simulations in Figures 3.3e-h show rings of high dot conductance that are in good agreement with the experimental images (Figures 3.3a-d). Changes in ring diameter with changing tip voltage accurately match the experimental images.

Maps of the tip induced shift in energy level vs. tip position obtained from the lineshape of the Coulomb blockade rings in Figures 3.3a-d are shown in Figures 3.3i-l. These maps were determined in the following way. For resonant tunneling, the lineshape is given by [3]

$$G = G_{max}[Cosh(\Delta_{E_F}/2k_BT)]^{-2} \tag{3.1}$$

where Δ_{E_F} is the energy difference between the lowest energy level in the dot and the Fermi energy in the leads. The energy difference is zero at resonance and deviates from zero as the tip shifts the energy level upwards or downwards. The dot conductance at resonance is [3]:

$$G_{max}(\vec{r}_{tip}) = (e^2/4k_BT)\Gamma(\vec{r}_{tip}) \tag{3.2}$$

The tunneling rate $\Gamma(\vec{r}_{tip})$ alters as the tip is scanned above the dot, due to changes in the coupling between the tip and the point contacts, resulting in variations in G_{max} along the ring as seen in Figures 3.3a-d. The values of $G_{max}(\vec{r}_{tip})$ in equation(3.2) used to compute the maps were obtained from a smooth two-dimensional polynomial function that was fit to the measured values of G_{max} along the crest of the ring.

The strong dependence of the Coulomb blockade conductance on Δ_{E_F} allows us to measure the energy shift accurately.

If the SPM tip is sufficiently close to the 2DEG, at distances less that the width of the electron wavefunction $|\psi(\vec{r})|^2$, it is theoretically possible to extract the shape of the wavefunction inside the dot from SPM images [36]. The wavefunction $|\psi(\vec{r})|^2$ can be extracted from a map of the dot energy level shift $\Delta_{E_F}(\vec{r}_{tip})$, where $\Delta_{E_F}(\vec{r}_{tip})$ equals $\Delta E(\vec{r}_{tip})$ plus a constant determined by the side-gate voltage V_G. The tip voltage V_{tip} is adjusted to produce only a weak tip perturbation $\Phi_{tip}(\vec{r}, \vec{r}_{tip})$, the change in electrostatic potential due to the tip in the plane of the 2DEG. From first-order perturbation theory, $\Delta E(\vec{r}_{tip})$ is the convolution of the wave function of the electron in the dot and the tip potential:

$$\Delta E(\vec{r}_{tip}) =< \psi(\vec{r})|\Phi_{tip}(\vec{r}, \vec{r}_{tip})|\psi(\vec{r}) >= \int \Phi_{tip}(\vec{r} - \vec{r}_{tip})|\psi(\vec{r})|^2 d\vec{r} \qquad (3.3)$$

Knowing the shape of $\Phi_{tip}(\vec{r}, \vec{r}_{tip})$, one can deconvolve measurements of $\Delta E(\vec{r}_{tip})$ using equation(3.3) to extract the shape of the unperturbed wavefunction amplitude $|\psi(\vec{r})|^2$. For the images presented in this paper, the tip perturbation was wider than the wavefunction, and this method is not applicable. In future experiments we hope to extract the shape of the wavefunction using a relatively narrow tip perturbation.

Chapter 4

Imaging the wavefunction amplitude of electrons inside quantum dots

4.1 Introduction

Mesoscopic devices offer a variety of possibilities for studying quantum mechanical effects in small dimensions. A complete understanding of a mesoscopic system is only possible if the wavefunction that describes the system is known. Any observable property of the system can be calculated by applying the corresponding operator to the wavefunction. The shape and extent of the electronic wavefunction inside a quantum dot reflects the energetics of the electrons, the interactions between electrons and the coupling of electrons to the leads and to the environment. Coherence of electrons inside a quantum dot or a quantum dot circuit depends strongly on interactions with

the phonon or nuclear environments, which can be dependent on the extent of the wavefunction. In short, measuring the wavefunction, while remaining an experimental challenge, contributes greatly to the understanding of mesoscopics and to improving the design and applications of mesoscale devices.

We propose a Coulomb blockade based scanning probe microscopy (SPM) method to image the wavefunction of electrons inside quantum dots, which combines electrical transport measurements and scanning gate microscopy. While conventional transport measurements on mesoscopic systems provide spectroscopic information, they offer little opportunity for obtaining spatial information about the electrons confined to a particular device. SPM provides a technique to spatially probe the electrons inside small structures. We take advantage of the accuracy with which low noise transport measurements on quantum dots give the energetics of the electrons, and the flexibility of scanning gate microscopy to be used with a variety of mesoscopic devices. Although our discussions in this chapter are limited to lateral quantum dots formed by surface gates in GaAs heterostructures, this technique can be easily extended to any quantum mechanical system that shows Coulomb blockade, including quantum dots formed in semiconductor nano-wires and other semiconductor heterostructures.

Our proposed technique allows us to extract the wavefunction of electrons trapped inside a quantum dot and buried underneath the surface. Scanning tunneling microscopy (STM) can be used to probe the wavefunction of electrons on surfaces by measuring tunneling rates the surface at a particular point underneath the tip. An STM was used to image the wavefunction of electrons confined to an elliptical resonator on a Cu surface, showing quantum mirage effect for a Co atom [37]. The elec-

tronic wavefunction in a metallic single-walled carbon nanotube was measured using STM, and spatial patterns reflecting the electronic structure of a single graphite sheet were observed [38]. Electrons inside quantum dot structures can also be probed using magneto-tunneling spectroscopy, which measures the tunneling rate into a particular point in k-space and uses a magnetic field to scan that point. Magneto-tunneling spectroscopy was used to measure the wavefunction of electrons inside self-assembled GaAs quantum dots [39].

Our proposed technique is based on resonant tunneling spectroscopy combined with SPM to induce local perturbations in the system. Wavefunction mapping using resonant tunneling as a measurement tool was discussed in theoretical papers for an open quantum dot [40] and for a quantum well [41]. Prior to using SPM as a local probe, local perturbations grown inside the samples were used as a means to probe quantum mechanical systems. The wavefunction of electrons inside a rectangular quantum well was first measured using a local perturbation formed by a mono-layer of Al atoms epitaxially grown at a fixed position inside the quantum well. Since the position of the perturbation was fixed, a series of quantum wells were measured with probes grown at different positions inside the well and optical spectroscopy was used to measure the wavefunction amplitude [42]. In a later experiment by G. Salis *et.al.* [43] a similar probing technique was used to image the wavefunction inside a parabolic quantum well. Taking advantage of the fact that a parabolic potential does not change its shape when placed in a constant electric field, the potential well could be moved relative to the probe by changing the voltage across the well, and preparation of multiple samples could be avoided. Using a scanning

gate microscope to induce a perturbation naturally follows the experiments mentioned above, making this technique applicable to a larger set of systems and providing a much more flexible probing technique where the position and magnification of the perturbation can be changed easily. Although the very small monolayer size of an epitaxially grown perturbation is hard to achieve with an SPM, the overall flexibility of SPM and its ability to fit to a variety of mesoscopic systems makes it a great candidate for measuring the wavefunction.

It is important to note that in all the experiments mentioned above as well as in our proposed technique the amplitude of the wavefunction or the probability density is the measured quantity. Extracting information about the phase of the wavefunction is very difficult, and has to be achieved through some form of interference or scattering measurement. A great example of such a measurement is the images obtained of coherent electron flow from a quantum point contact in a 2 dimensional electron gas (2DEG) [22, 23] where coherent oscillations were observed in the flow images due to the interference of back-scattered electrons from a tip induced scatterer.

In the previous chapter we experimentally demonstrated imaging of electrons in a few-electron quantum dot using a liquid He temperature SPM. In this chapter we use numerical simulations to demonstrate how this technique can be used to extract information about the electronic wavefunction inside the quantum dot. In the first part of the chapter the origin of the conductance images are explained and images of the one-electron ground state and excited states are simulated for a symmetric harmonic potential and an elongated quantum dot. In the following sections the procedure for extracting the wavefunction is described and the requirements for utilizing

the technique are explained. Finally the wavefunction extraction method is applied to the experimental images described in chapter 3 and the validity of the results are discussed.

4.2 Coulomb blockade imaging technique

Coulomb blockade images of electrons are obtained by scanning a charged SPM tip at a fixed height above the quantum dot while simultaneously measuring the conductance through the quantum dot as a function of tip position. A voltage V_{tip} is applied between the conductive SPM tip and the quantum dot. The dot is tuned in the few-electron Coulomb blockade regime, where conductance through the discrete energy levels inside the quantum dot is allowed only if enough energy is provided for the electrons in the leads to overcome the Coulomb energy associated with the electrons inside the quantum dot. In other words a conductance peak occurs when the chemical potential inside the dot is aligned with the chemical potential of the leads.

As a charged tip approaches the quantum dot it capacitively couples to the quantum dot and changes the potential that forms the dot, $\phi(x, y)$. Figure 4.1a shows a schematic of the dot potential $\phi(x, y)$ along the x-axis before (blue trace) and after (red trace) a charged tip is introduced. Here $\phi(x, y)$ is assumed to be a two dimensional harmonic potential with a resonance frequency ω_0, where $\hbar\omega_0 = 3$ meV and is close to that of realistic quantum dot devices such as the one measured in the previous chapter.

The green trace in figure 4.1a shows the potential due to an SPM tip along the

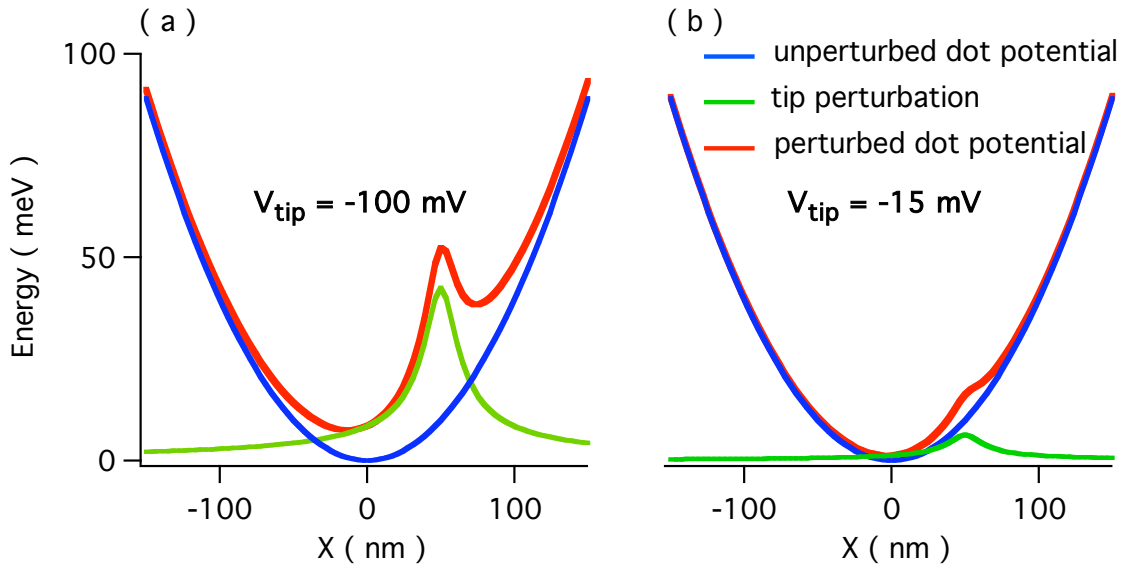

Figure 4.1: A cross section of the potential forming the quantum dot is shown before (blue trace) and after (red trace) a charged SPM tip is introduced. The dot potential is assumed to have a two dimensional harmonic form with a resonance frequency ω_0, where $\hbar\omega_0 = 3$ meV. The green trace shows a cross section of the potential due to a charged SPM held at $H_{tip} = 10$ nm and at a voltage (a) $V_{tip} = -100$ mV and (b) $V_{tip} = -15$ mV. A charged sphere model is used to calculate the tip potential, where the radius of the sphere is given by the SPM tip radius of curvature (30 nm) and the voltage and height of the sphere are given by V_{tip} and H_{tip}. The red trace shows the perturbed dot potential along the x-axis. The amplitude of the perturbation can be tuned by changing V_{tip} as shown above.

x-axis, with a voltage $V_{tip} = -100$ mV held at $H_{tip} = 10$ nm above the quantum dot. The tip potential is calculated assuming it is similar to that of a charged sphere with a voltage V_{tip} held at H_{tip} above the surface of the heterostructure containing the quantum dot. The radius of the sphere is equal to the radius of curvature of the SPM tips used for our images, i.e. 30nm. If the size of the tip perturbation is small compared to the dot potential, the tip introduces a local perturbation in the dot potential as observed in figure 4.1. The amplitude of this perturbation is given by the amplitude of the tip potential, and can be tuned by changing the tip voltage, V_{tip}. Figure 4.1b shows the dot potential with an SPM tip held at $V_{tip} = -15$ mV and $H_{tip} = 10$ nm. The size of the perturbation is the same as that of figure 4.1a however the amplitude of the perturbation is 10 times smaller. Note that all parameters used in these simulations are similar to the experimental values except for the tip height H_{tip}. A smaller value for H_{tip} is chosen to enhance the imaging resolution, as needed for the purpose of this chapter. The resolution requirements are discussed in more detail later in this chapter.

Imaging a quantum dot with symmetric harmonic potential

Figure 4.2a-d plots the charge density or the amplitude squared of the wavefunctions associated with the ground state and three excited states in a symmetric two-dimensional harmonic potential. The two-dimensional harmonic potential has a resonance frequency ω_0 where $\hbar\omega_0 = 3$ meV. The quantum numbers (n,m) for the states plotted in figure 4.2a-d are shown in parenthesis, where n is the energy quantum number and m is the angular quantum number. The angular momentum quantum

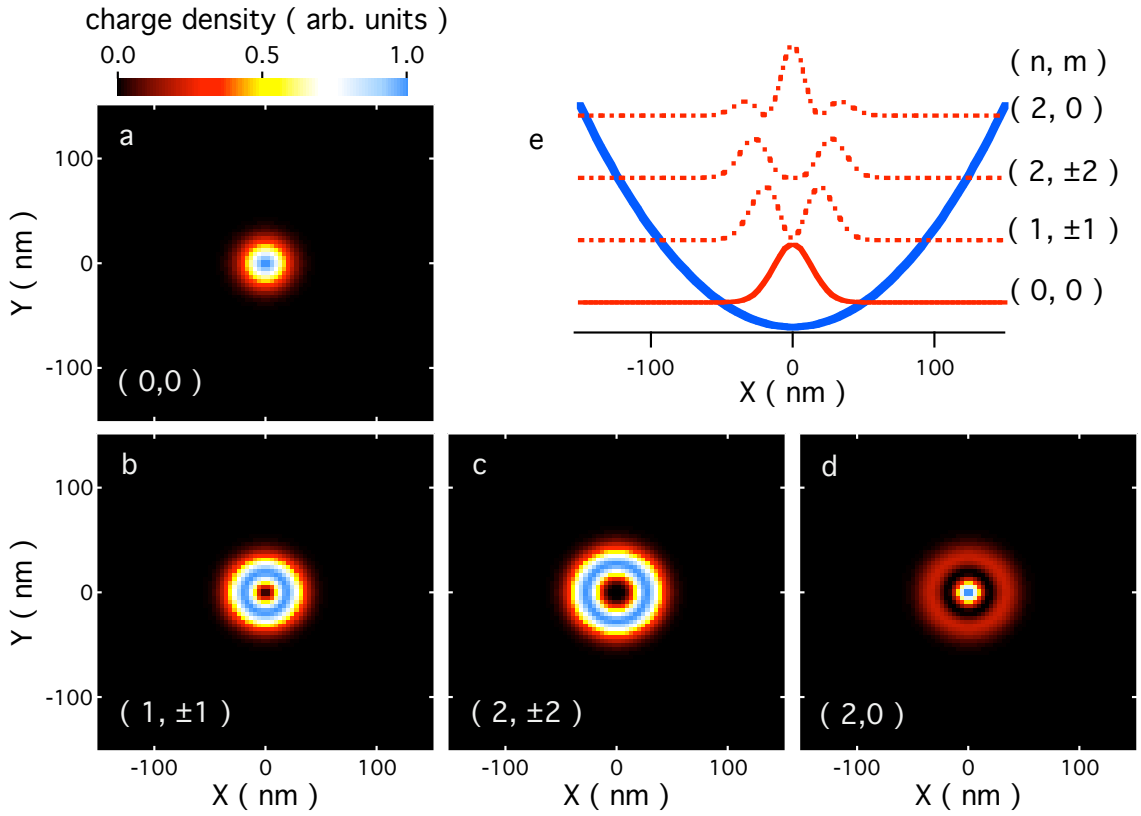

Figure 4.2: (a-d) Plots of the charge density (square amplitude of the wavefunction) for the ground state and three excited states in a two-dimentional harmonic potential with $\hbar\omega_0 = 3$ meV. (e) The harmonic potential along the x-axis (blue trace) and the charge densities of the ground state (solid red trace) and the excited states (dashed red traces).

number is a good quantum number due to the circular symmetry of the dot potential. The ground state has a peak in density in the center while the excited states show a ring around the center with or without a peak in the center. Figure 4.2e shows the harmonic dot potential along the x-axis and the charge densities of the (0,0) ground state and the excited states. The diameter of the outer ring expands as the energy increases. The excited states $(2, 0)$ and $(2, \pm 2)$ are degenerate in energy while having different radial wavefunctions. We'll discuss the effect of this degeneracy on the images later in this chapter.

As the SPM tip is scanned above the quantum dot it changes the dot energy and shifts the chemical potential inside the quantum dot. As discussed before conductance through the quantum dot is allowed only if the chemical potential inside the dot is aligned with that of the leads. The SPM tip can therefore bring the dot in or out of resonance with the leads and change the conductance through the quantum dot as it is scanned above it. The SPM images are plots of dot conductance as a function of tip position. Figure 4.3 shows a series of simulated images of a quantum dot represented by the harmonic potential of figure 4.2. In these images conductance occurs only through the (0,0) ground state because the other states are energetically not available. The images in figure 4.3 are obtained with different tip voltages. As the tip voltage is made more negative it changes the dot chemical potential more strongly and cause the images to alter. Figures 4.4 and 4.5 show images obtained of the $(2, 0)$ and $(2, 2)$ excited states respectively. A similar change with tip voltage is observed for all these images. Furthermore slight differences in the figures 4.3, 4.4 and 4.5 are observed for smaller gate voltages reflecting properties of the wavefunctions.

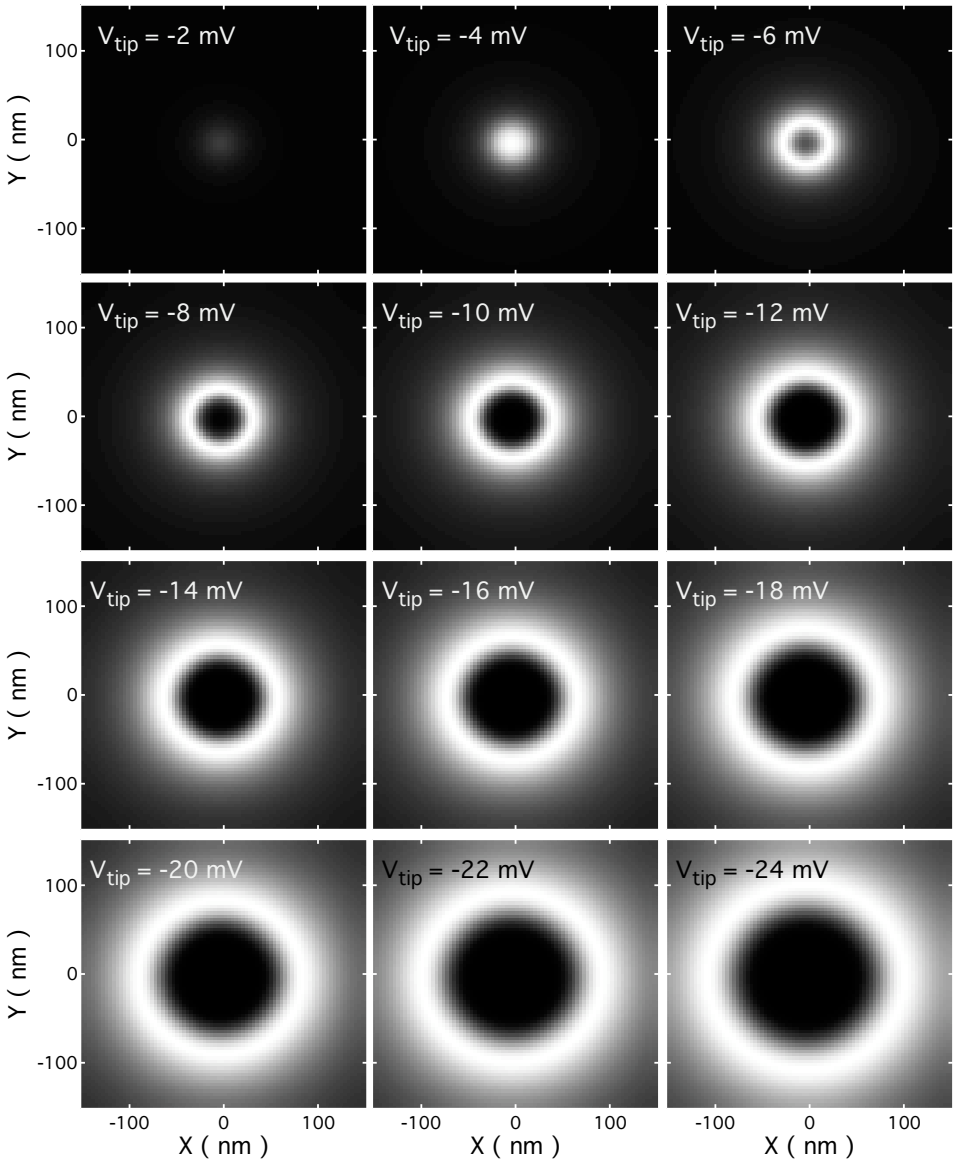

Figure 4.3: Simulated Coulomb blockade conductance images though the (0,0) ground state of quantum dot with a symmetric two-dimentional harmonic potential ($\hbar\omega_0 = 3$ meV). The images are plots of dot conductance as a function of tip position. The tip is scanned 10 nm above the quantum dot and the tip voltage is between -2 mV and -24 mV for the different figures.

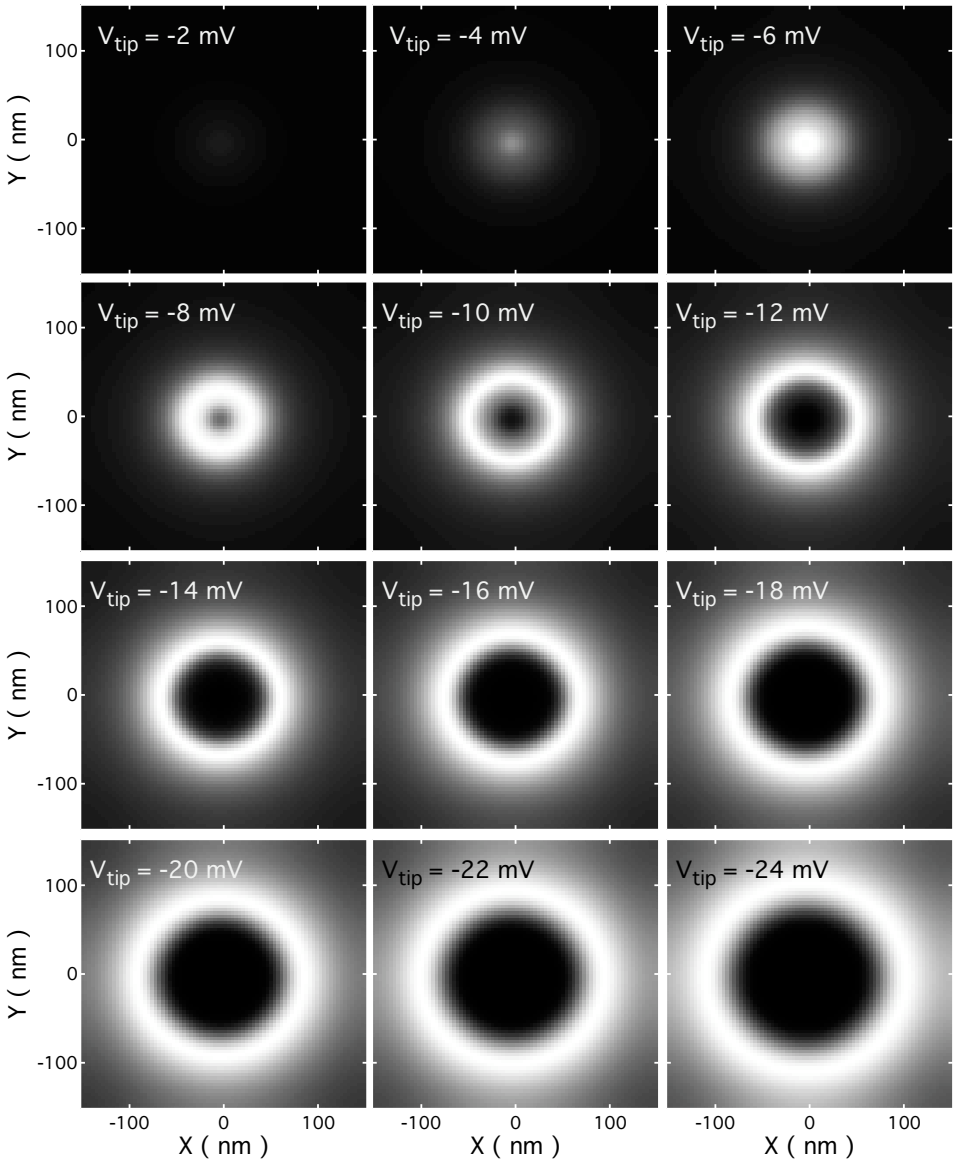

Figure 4.4: Simulated Coulomb blockade conductance images though the (2,0) excited state of quantum dot with a symmetric two-dimentional harmonic potential ($\hbar\omega_0 = 3$ meV). The images are plots of dot conductance as a function of tip position. The tip is scanned 10 nm above the quantum dot and the tip voltage is between -2 mV and -24 mV for the different figures.

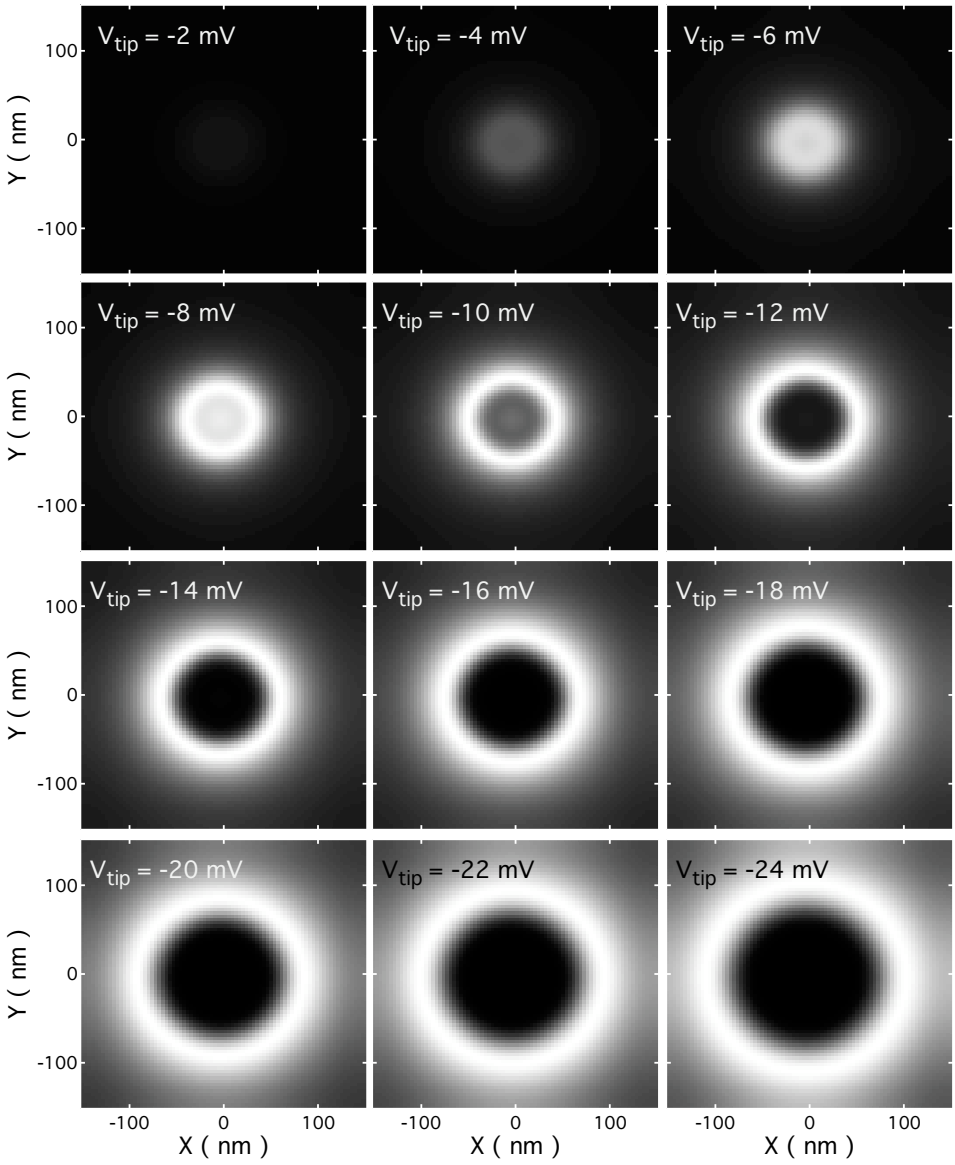

Figure 4.5: Simulated Coulomb blockade conductance images though the (2,2) excited state of quantum dot with a symmetric two-dimentional harmonic potential ($\hbar\omega_0 = 3$ meV). The images are plots of dot conductance as a function of tip position. The tip is scanned 10 nm above the quantum dot and the tip voltage is between -2 mV and -24 mV for the different figures.

To fully explain the images we need to understand how the tip affects the dot energy. The change in the energy levels inside the quantum dot as the SPM tip is introduced can be estimated using first order perturbation theory, which states the change in the energy of a state ΔE to first order is given by the expectation value of the perturbation potential $\Phi_{perturbation}$:

$$\Delta E =< \psi|\Phi_{perturbation}|\psi > \tag{4.1}$$

where ψ is the wavefunction associated with that state.

In case of a quantum dot perturbed by a charged SPM tip, $\Phi_{perturbation}$ is the tip potential $\Phi_{tip}(\vec{r}_{tip})$, where $\vec{r}_{tip}$ is the tip position. We can rewrite equation 4.1 as:

$$\Delta E(\vec{r}_{tip}) =< \psi(\vec{r})|\Phi_{tip}(\vec{r},\vec{r}_{tip})|\psi(\vec{r}) >= \int \Phi_{tip}(\vec{r}-\vec{r}_{tip})|\psi(\vec{r})|^2 d\vec{r} \tag{4.2}$$

The change in an energy level inside the quantum dot is therefore given by the convolution of the tip potential and the squared amplitude of the wavefunction associated with that energy state. Figure 4.6 plots ΔE (dashed trace) along the x-axis together with the tip perturbation (green trace) and the amplitude squared of the wavefunction (red trace) for the (0,0) and (2,2) states. If the tip perturbation is smaller or of the same size as the wavefunction we can clearly see features corresponding to the wavefunction in plots of ΔE, which are then reflected in the conductance images. Note that for the wavefunctions discussed here the similar circular symmetry of the tip potential and the wavefunctions prevents the features associated with the wavefunction to stand out in the conductance images. In the next section we discuss an elongated quantum dot where the wavefunction features are much more visible in the conductance images.

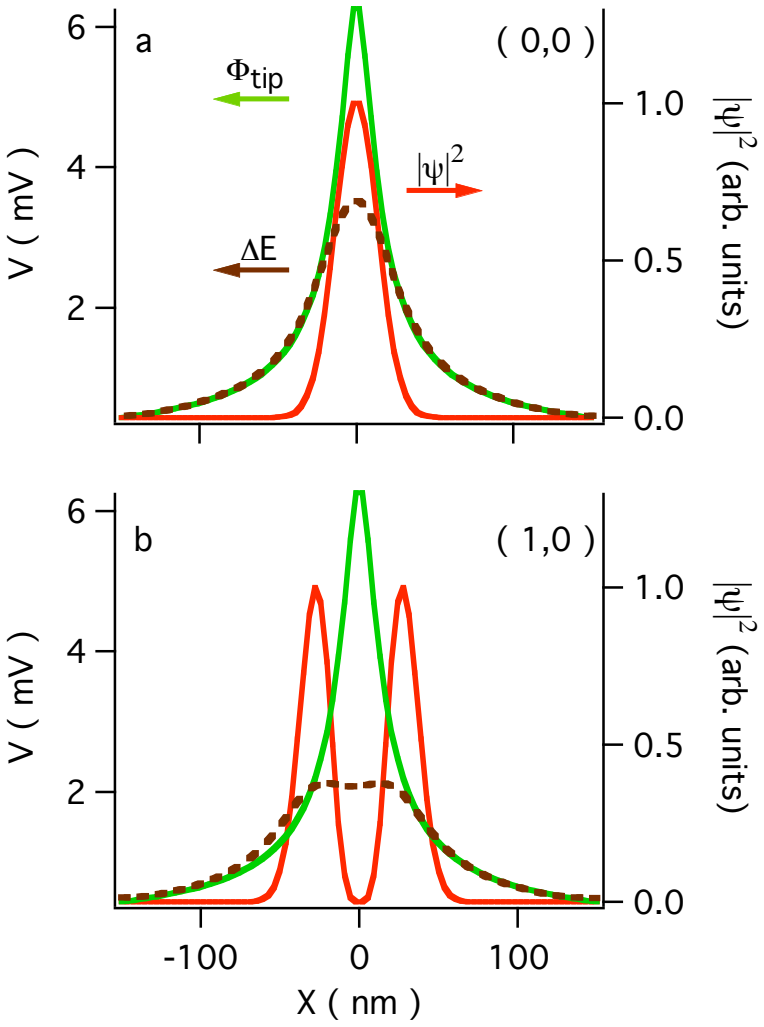

Figure 4.6: Plots of ΔE, the change in the dot energy level at a function of tip position for (a) the (0,0) ground state and (b) the (2,2) excited state (dashed brown trace). The dot is assumed to have a symmetric harmonic potential with $\hbar\omega_0 = 3$ meV. The tip potential (green trace) and the square amplitude of the wavefunction (red trace) are also plotted for each state. The change in the dot energy, ΔE, is a convolution of the tip potential and the square amplitude of the wavefunction.

The energy of each state inside the dot $E(\vec{r}_{tip})$ can be calculated for any tip position $\vec{r}_{tip}$ using equation 4.2, and is given by:

$$E(\vec{r}_{tip}) = E_0 + \Delta E(\vec{r}_{tip}) = E_0 + \int \Phi_{tip}(\vec{r} - \vec{r}_{tip})|\psi(\vec{r})|^2 d\vec{r} \tag{4.3}$$

where E_0 is the energy of that state without the tip present and ψ is the wavefunction associated with that state.

Conductance through the quantum dot can be obtained using the calculated dot energy if the line-shape of a Coulomb blockade peak in known. Conductance is allowed when an energy state is aligned with the Fermi energy of the leads. As the dot energy levels are shifted by the SPM tip or by a gate voltage a peak in conductance is observed as energy levels come into resonance with the leads. The line-shape of this peak is dependent on various factors including temperature, tunneling rates through the barriers and the dot energy level spacing. We assume the dot is tuned in the resonant tunneling regime where tunneling occurs through an individual state in the dot and the conductance peaks are temperature broadened. The line-shape of a Coulomb blockade peak in this regime is given by [3]

$$G = G_{max}[Cosh(\Delta_{E_F}/2k_BT)]^{-2} \tag{4.4}$$

where G_{max} is the dot conductance at resonance given by the temperature and the tunneling rates through the barriers [3], and Δ_{E_F} is the energy difference between the dot energy level and the Fermi energy of the leads E_F, given by:

$$\Delta_{E_F}(\vec{r}_{tip}) = E(\vec{r}_{tip}) - E_F = E_0 + \Delta E(\vec{r}_{tip}) - E_F = E_0 - E_F + \int \Phi_{tip}(\vec{r} - \vec{r}_{tip})|\psi(\vec{r})|^2 d\vec{r} \tag{4.5}$$

If the dot is tuned in a different Coulomb blockade regime the conductance can be calculated only if we know the form of the Coulomb blockade line-shape in that regime.

The conductance images through particular states inside a quantum dot (figures 4.3, 4.4 and 4.5) are constructed by calculating the dot energy at each value of $\vec{r}_{tip}$ from equantion 4.3 and calculating the conductance through the dot from equation 4.4 and 4.5. Areas of high conductance occur when the dot is in resonance with the leads and correspond to contours of constant dot energy, or constant tip to dot coupling. We expect the images to have features that correspond to the wavefunction of the state through which conductance occurs, since the dot energy (equation 4.3) depends on the convolution of the tip perturbation and the amplitude squared of the wavefunction and mimics features from the wavefunction as seen on figure 4.6. However, as mentioned before, for a circularly symmetric dot potential with circularly symmetric wavefunctions these features are hard to distinguish, explaining the similarity between the images shown in figures 4.3, 4.4 and 4.5. The elongated quantum dot discussed in the next section demonstrates much stronger evidence of the wavefunction pattern in the conductance images.

When imaging degenerate states, conductance can potentially occur through more than one state. In a quantum dot with circular symmetry, states with energy quantum number n, are n+1 fold degenerate. For example, the states (2,0) and $(2, \pm 2)$ shown in figure 4.2 all have an energy of $3\hbar\omega_0$. Degenerate states with the same radial wavefunction, i.e. states with the same energy quantum number n and angular momentum numbers of opposite sign $\pm$m, differ only in the phase of the wavefunction

$e^{im\phi}$, and look the same in conductance images since this technique is not sensitive to phase. However we expect degenerate states with different radial quantum numbers to have different conductance images. As the tip is scanned above the quantum dot it shifts the energy level of the states with different radial wavefunctions by different amounts as shown by equation 4.2. Therefore when a tip is brought close to a quantum dot with degenerate states it lifts the degeneracy. At any tip position $\vec{r}_{tip}$ conductance occurs only through the state that is brought in resonance with the leads, as if there was no degeneracy to begin with. For special values of tip position, where more than one state are in resonance with the leads, electrons tunnel through one state at a time in a random order. Note that only one electron can be on the dot at a particular time, once one electron is added the other degenerate states are no longer energetically available due to the charging energy associated with the added electron. From this simple picture of electrons tunneling through the quantum dot we expect to see a superposition of conductance images corresponding to each state when imaging degenerate states with different radial wavefunctions.

What was so far discussed in this chapter is correct in a non-interacting electron picture for a quantum dot with one or many electrons. When a tip is brought close to a quantum dot that contains more than one electron, it changes the energies of all the levels that are already filled and hence changes the total dot energy. However the conductance is only sensitive to the changes of the energy level through which tunneling is happening and does not detect the changes in the states that are already full. If electron-electron interactions are included the picture becomes more complicated. The tip can screen the interactions and change the energy level that

is probed not only through perturbing the potential but also through perturbing the electron-electron interactions. However since the tip is relatively far from the dot we expect the influence of the tip on electron-electron interactions to be small.

Imaging elongated quantum dots

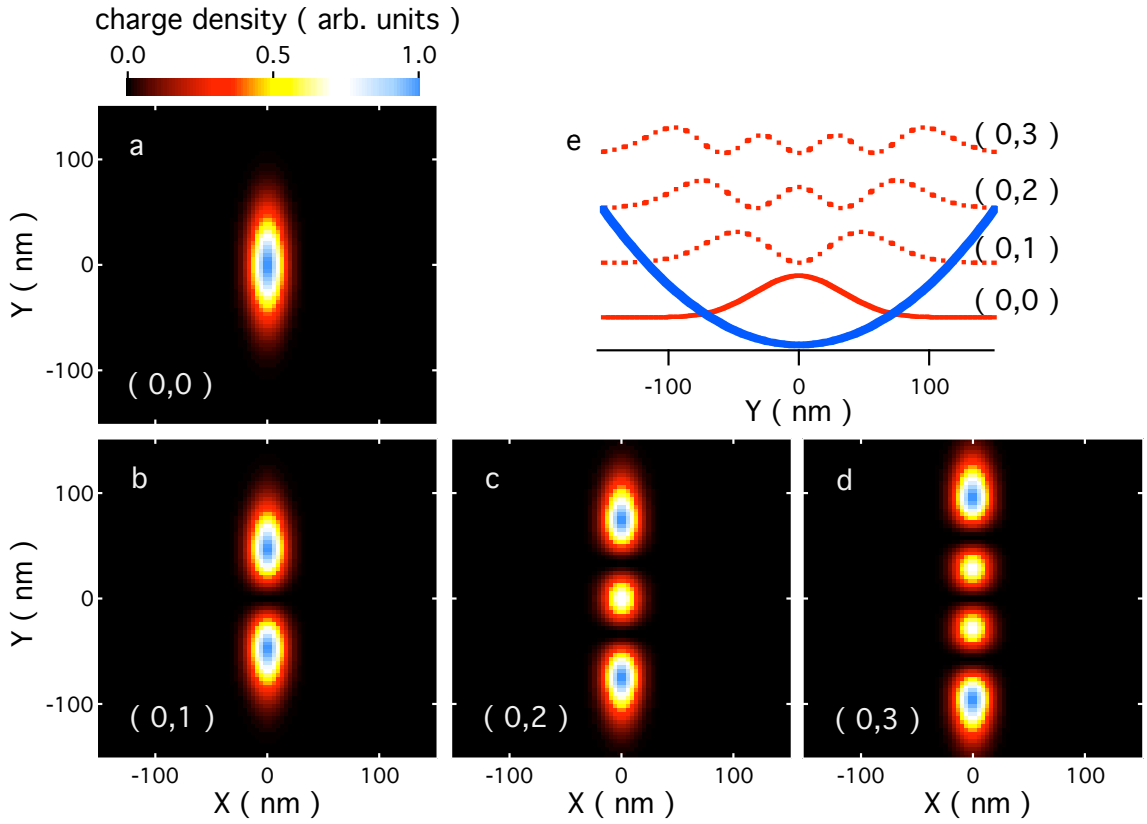

Figure 4.7: (a-d) Plots of the charge density (square amplitude of the wavefunction) for the ground state and the first three orbital excited states in an elongated two-dimentional harmonic potential with $\hbar\omega_1 = 5$ meV and $\hbar\omega_2 = 0.5$ meV. (e) The harmonic potential along the y-axis (blue trace) and the charge densities of the ground state (solid red trace) and the (0,1), (0,2) and (0,3) excited states (dashed red traces).

The Coulomb blockade imaging technique can be applied to quantum dots of different shapes. Figure 4.7a-d shows plots of the amplitude squared of the wave-

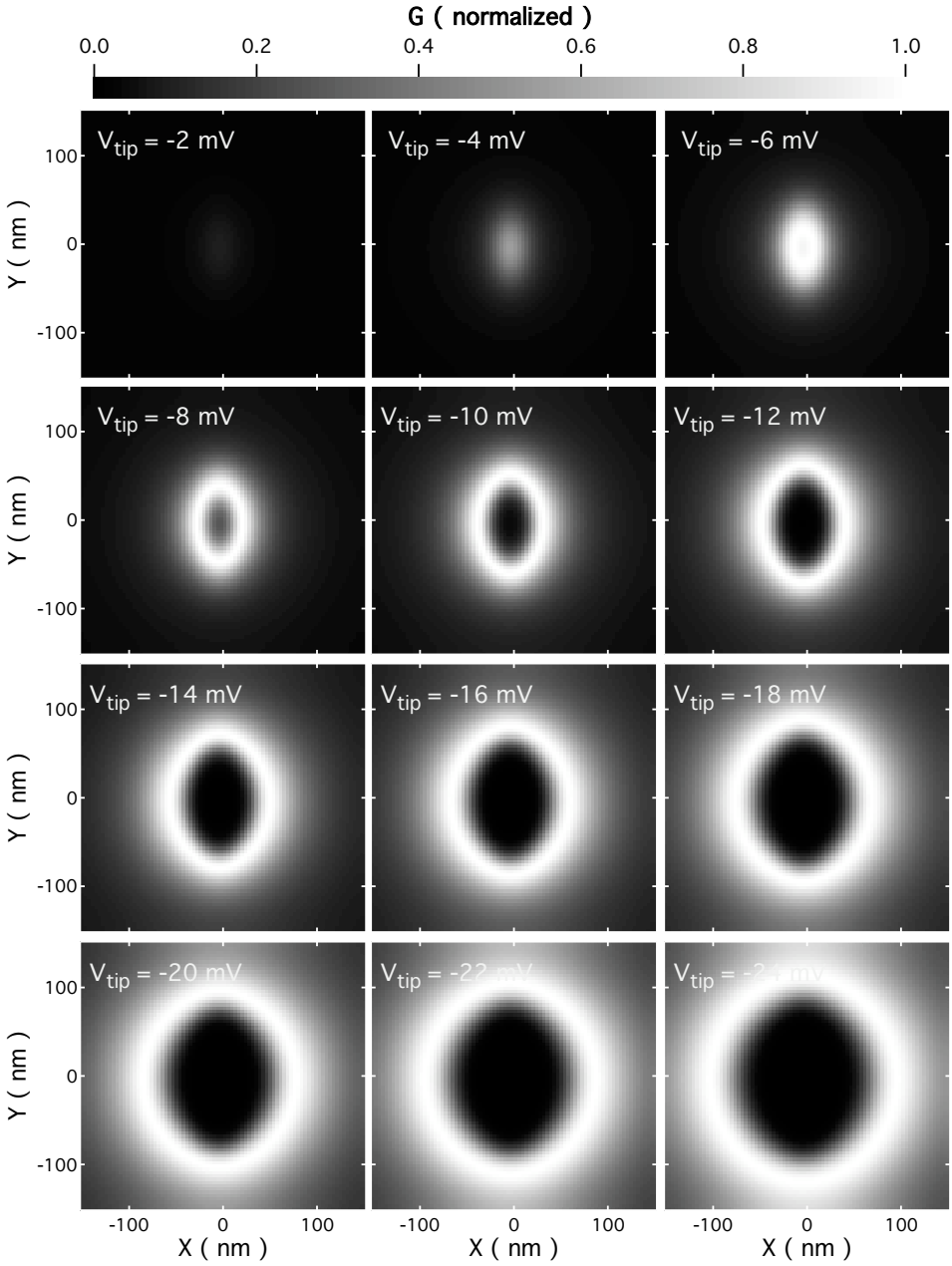

Figure 4.8: Simulated Coulomb blockade conductance images though the (0,0) ground state of quantum dot with an elongated two-dimentional harmonic potential ($\hbar\omega_1 = 5$ meV, $\hbar\omega_2 = 0.5$ meV). The images are plots of dot conductance as a function of tip position. The tip is scanned 10 nm above the quantum dot and the tip voltage is between -2 mV and -24 mV for the different figures.

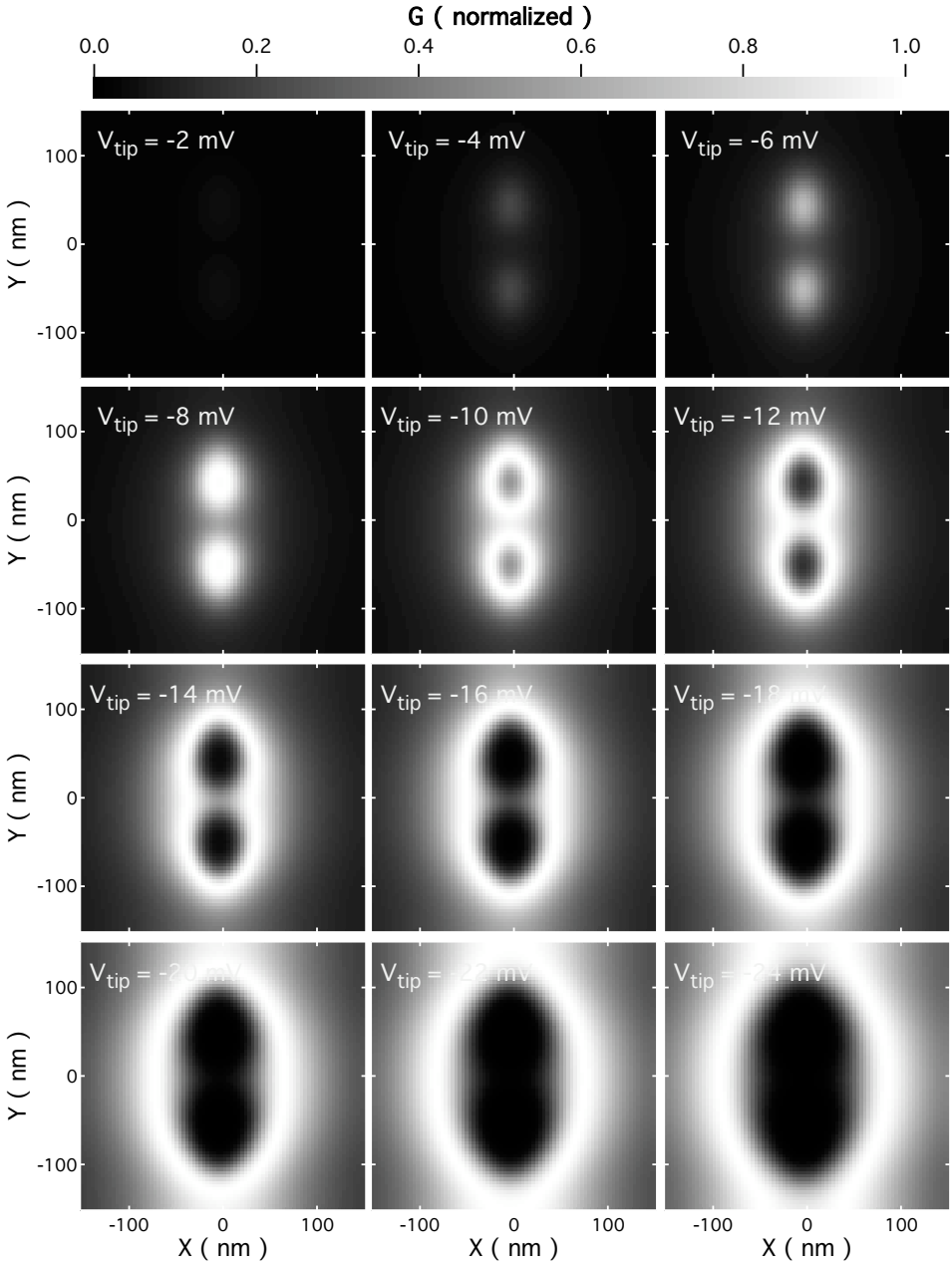

Figure 4.9: Simulated Coulomb blockade conductance images though the (0,1) excited state of quantum dot with an elongated two-dimentional harmonic potential ($\hbar\omega_1 = 5$ meV, $\hbar\omega_2 = 0.5$ meV). The images are plots of dot conductance as a function of tip position. The tip is scanned 10 nm above the quantum dot and the tip voltage is between -2 mV and -24 mV for the different figures.

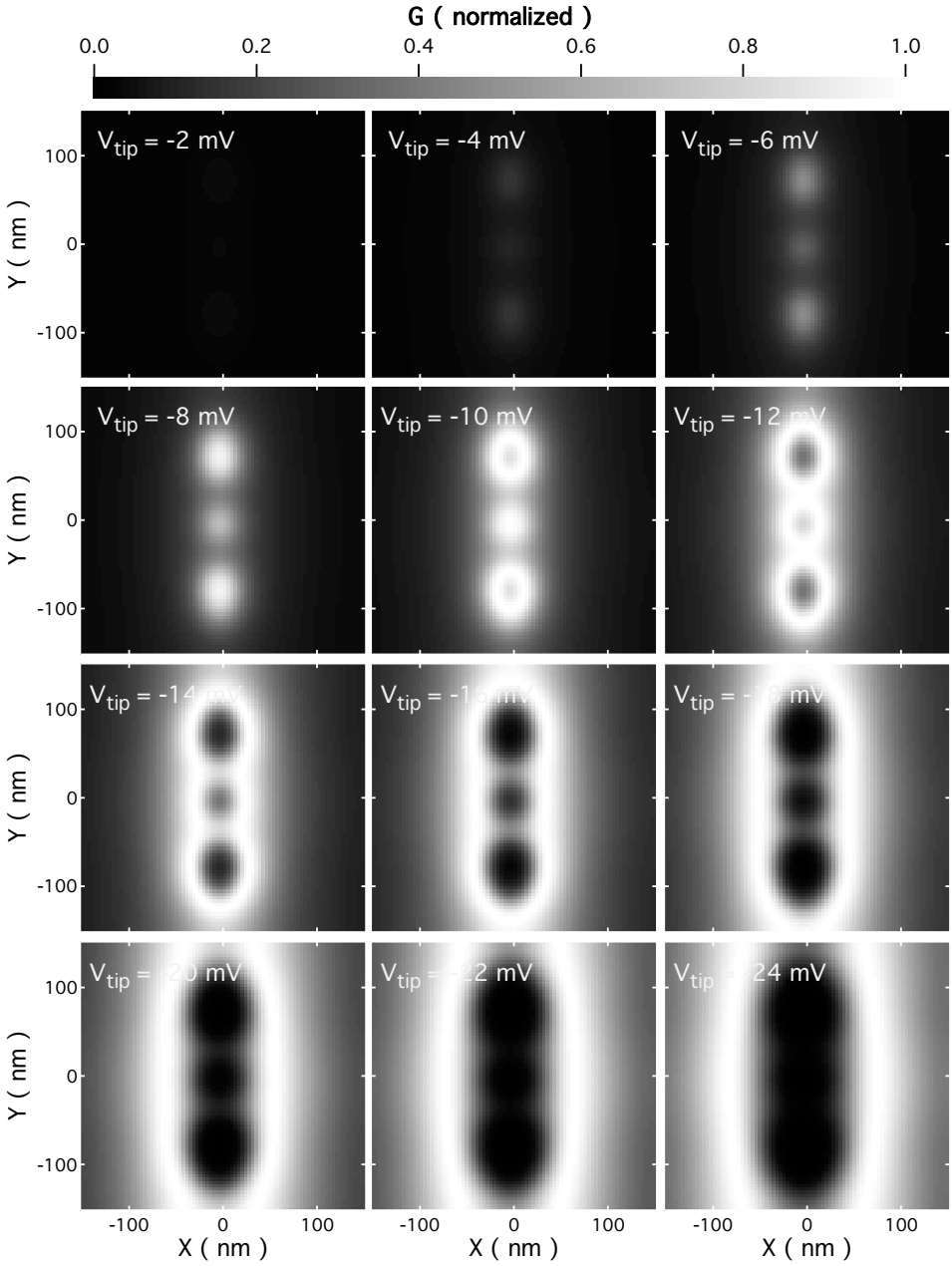

Figure 4.10: Simulated Coulomb blockade conductance images though the (0,2) excited state of quantum dot with an elongated two-dimentional harmonic potential ($\hbar\omega_1 = 5$ meV, $\hbar\omega_2 = 0.5$ meV). The images are plots of dot conductance as a function of tip position. The tip is scanned 10 nm above the quantum dot and the tip voltage is between -2 mV and -24 mV for the different figures.

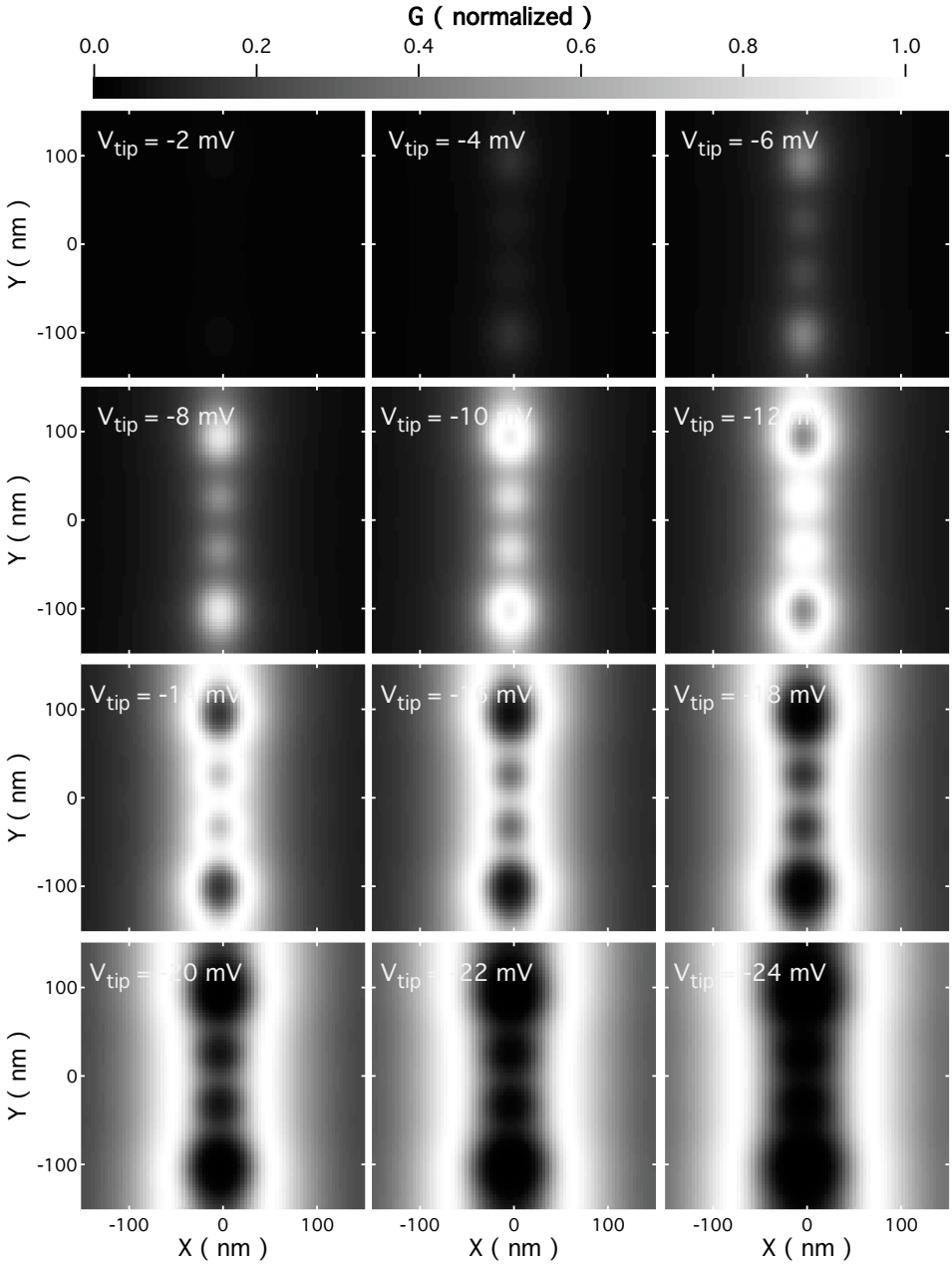

Figure 4.11: Simulated Coulomb blockade conductance images though the (0,3) excited state of quantum dot with an elongated two-dimentional harmonic potential ($\hbar\omega_1 = 5$ meV, $\hbar\omega_2 = 0.5$ meV). The images are plots of dot conductance as a function of tip position. The tip is scanned 10 nm above the quantum dot and the tip voltage is between -2 mV and -24 mV for the different figures.

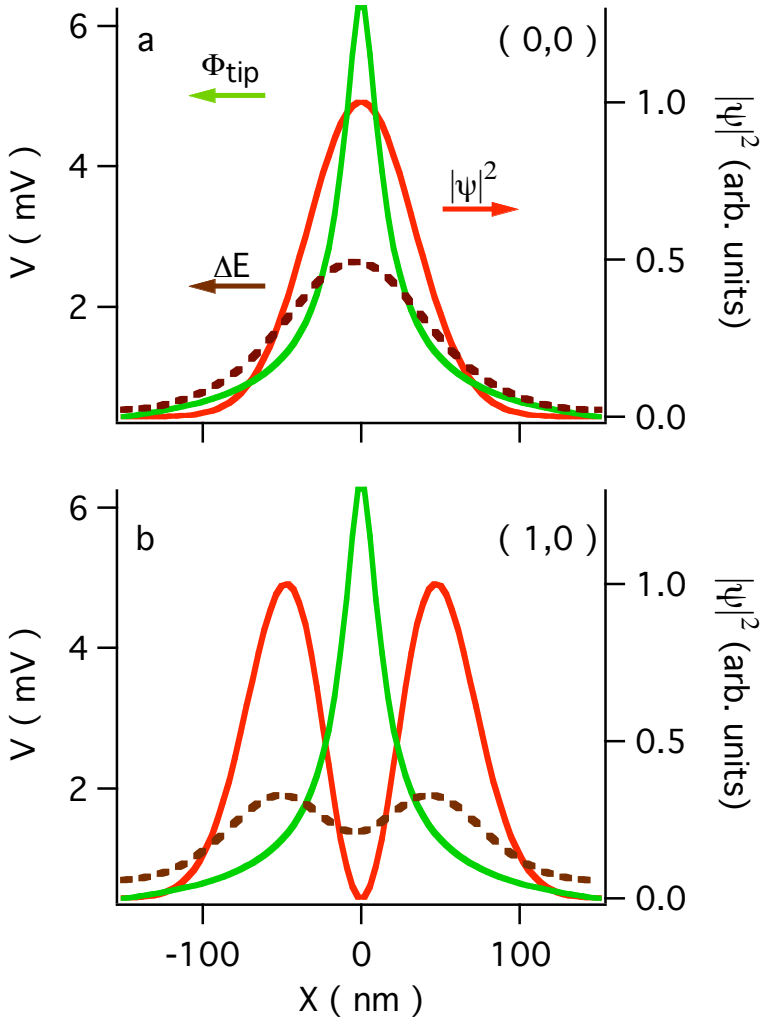

Figure 4.12: Plots of ΔE, the change in the dot energy level at a function of tip position for (a) the (0,0) ground state and (b) the (1,0) excited state (dashed brown trace). The dot is assumed to have an elongated harmonic potential with $\hbar\omega_1 = 0.5$ meV and $\hbar\omega_1 = 5$ meV. The tip potential (green trace) and the square amplitude of the wavefunction (red trace) are also plotted for each state. The change in the dot energy, ΔE, is a convolution of the tip potential and the square amplitude of the wavefunction.

function of the ground state and the first three orbital excited states in an elongated dot potential. The dot potential here is a two-dimensional harmonic potential with two different resonance frequencies ω_1 and ω_2, where $\hbar\omega_1 = 5$ meV and $\hbar\omega_2 = 0.5$ meV. The eigenstates of an asymmetric two-dimensional harmonic oscillator are given by multiplications of the eigenstates of one-dimensional harmonic oscillators in each coordinate x and y. The quantum numbers in parenthesis are the energy quantum numbers associated with the eigenstates in x and y respectively. The confinement is much stronger in one direction compared to the other and therefore the first three orbital excited states are the (0,1), (0,2) and (0,3) states. A rich structure is observed in the plots of the squared wavefunction amplitude, showing an additional peak along the direction of lower confinement for each excited state.

Figures 4.8, 4.9, 4.10 and 4.11 show simulated conductance images obtained of the ground state and the first three excited states in the elongated quantum dot. For small tip voltages, where the change in the dot energy is small, the images show features corresponding to the shape of the wavefunction. This is expected since the dot energy (equation 4.3) depends on the convolution of the tip perturbation and the amplitude squared of the wavefunction. As the tip voltage is made more negative the change in the dot energy is such that resonance is achieved when the tip is further away from the quantum dot and therefore the fine features of the wavefunction are not as obvious, however the overall elongated shape of the quantum dot is reflected in the images.

Figure 4.12 plots ΔE (dashed trace) along the x-axis together with the tip perturbation (green trace) and the amplitude squared of the wavefunction (red trace)

for the (0,0) and (1,0) states. For an elongated quantum dot the ratio of tip size to the size of the wavefuntion in the direction of lower confinement is small compared to a symmetric dot, resulting in an enhanced imaging resolution in that direction as discussed later in this chapter.

4.3 Extracting the wavefunction

The goal of this chapter is to demonstrate how we can extract the amplitude of the wavefunction using our Coulomb blockade imaging technique. So far we have demonstrated how the images are formed and how the convolution of the tip potential and the wavefunction amplitude plays a significant role in their formation. At this point it should be obvious how by following the steps to construct the images in the reverse order we can extract the wavefunction amplitude.

The first step is to calculate ΔE, the change in the dot energy, from the conductance images. We can do so by taking the reverse of equation 4.4 and 4.5:

$$\Delta_{E_F}(\vec{r}_{tip}) = 2k_BTCosh^{-1}(\sqrt{\frac{G_{max}}{G(\vec{r}_{tip})}}) = E(\vec{r}_{tip}) - E_F = E_0 + \Delta E(\vec{r}_{tip}) - E_F \quad (4.6)$$

So we have:

$$\Delta E(\vec{r}_{tip}) = \Delta_{E_F}(\vec{r}_{tip}) + E_F - E_0 = 2k_BTCosh^{-1}(\sqrt{\frac{G_{max}}{G(\vec{r}_{tip})}}) + E_F - E_0 \quad (4.7)$$

The values for $G(\vec{r}_{tip})$ are read from the images. The value for $E_F - E_0$ can be estimated from the position of a Coulomb blockade peak in a gate voltage sweep performed prior to the scanning. If there is no noise in the images, ΔE can be calculated for all values of $\vec{r}_{tip}$ from only one of the conductance images. Figure 4.13a

shows ΔE calculated from a conductance image (figure 4.13b) of the (1,0) excited state in an elongated quantum dot. The value for $E_F - E_0$ was chosen to be 1meV when constructing the images and the same value was used here to calculate ΔE. In the experiment this value can be tuned using one of the gate voltages. The plot of ΔE accurately resembles the energy change in the corresponding energy level given by the convolution of the tip perturbation and the wavefunction. Figures 4.13c and e show cross sections of plots a and b respectively along the $y = 0$ line.

If noise is present in the images, as in real experiments, ΔE can only be extracted for those values of $\vec{r}_{tip}$ at which the signal to noise ratio is high, i.e. areas of high conductance. More than one image might therefore be used to reconstruct ΔE for all values of $\vec{r}_{tip}$. To mimic a real experimental situation in the simulations, a randomly generated noise was added to the conductance images. Figure 4.13d shows cross sections of two conductance images obtained with different tip voltages indicated on the plot. The values of ΔE calculated from these images along the same axis is shown in figure 4.13f. In the conductance image obtained with $V_{tip} = 14$ mV, the signal to noise ratio is good along the x-axis except for the areas between the peaks indicated by the arrows. The values of ΔE calculated from this image behave similarly: the calculated values of ΔE are in good agreement with the actual values (shown on plot e) except for areas indicated by the arrows. To calculate ΔE along the x-axis we need to use another conductance image that has a better signal to noise ratio in the indicated areas, e.g. the image obtained with $V_{tip} = 6$ mV shown in blue on plot d. The values of ΔE calculated from this image agree well with the actual values in the central part of the trace but become very noisy towards the ends. Figure

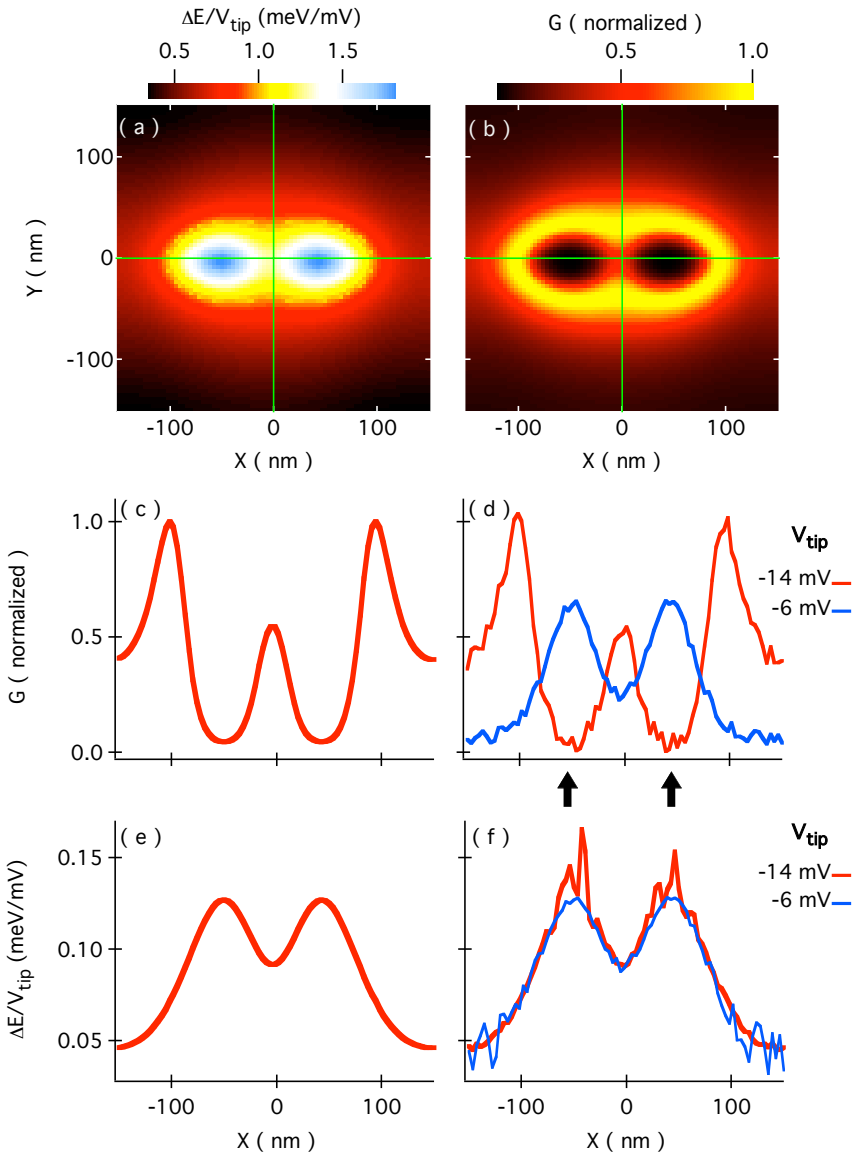

Figure 4.13: (a) plot of the change in the (1,0) energy level inside an elongated quantum dot as a function of tip position with a $V_{tip} = -14mV$. The value of ΔE plotted here are calculated from the conductance image in plot (b). (c) and (e) Cross sections of the plots shown in (b) and (a) respectively, along the y=0 line. (d) Cross sections of conductance images of the (1,0) state with tip voltages -10 and -6 mV for the red and blue traces respectively, and with a randomly generated noise added to mimic real experiments. The signal to noise ratio in the red trace is good along the x-axis except for areas indicated by the arrow. (f) Cross sections of the energy shift, ΔE, calculated from the conductance images of plot (d). The values of ΔE calculated from the red trace on (d) resemble the actual values well, except for the areas indicated by the arrows. In the presence of noise two conductance plots were needed to reconstruct the energy shift shown in plot (e).

4.13 demonstrates how multiple conductance images can be used to most accurately calculate ΔE for all values of $\vec{r}_{tip}$.

The second step towards extracting the wavefunction is to deconvolve ΔE with respect to the tip potential. From equation 4.2 we know that $\Delta E(\vec{r}_{tip})$ is a convolution of the tip potential $\Phi_{tip}(\vec{r}_{tip})$ and the squared amplitude of the wavefunction. Assuming $\Phi_{tip}(\vec{r}_{tip})$ is known to us, either from measurements or from simulations, we can deconvolve ΔE with respect to $\Phi_{tip}(\vec{r}_{tip})$ and extract the amplitude squared of the wavefunction.

Figure 4.14 shows plots of ΔE (third column) given by the convolution of the tip potential plotted in the second column and the wavefunction squared of the corresponding state plotted in the first column. The last column shows the result of the deconvolution of ΔE with respect to the tip potential. The deconvolution is numerically performed by taking the Fourier transforms of ΔE and of Φ_{tip} and dividing them together to get the Fourier transform of $|\psi|^2$:

$$FT[|\psi(\vec{r})|^2] = \frac{FT[\Delta E(\vec{r}_{tip})]}{FT[\Phi_{tip}(\vec{r} - \vec{r}_{tip})]} \tag{4.8}$$

As demonstrated in figure 4.14 the amplitude squared of the wavefunction is fully recovered through the deconvolution process.

4.4 Resolution

So far in this chapter we demonstrated that the SPM conductance images contain information about the wavefunction and can be used to extract the amplitude of the wavefunction. In this section we discuss the requirements for utilizing this technique.

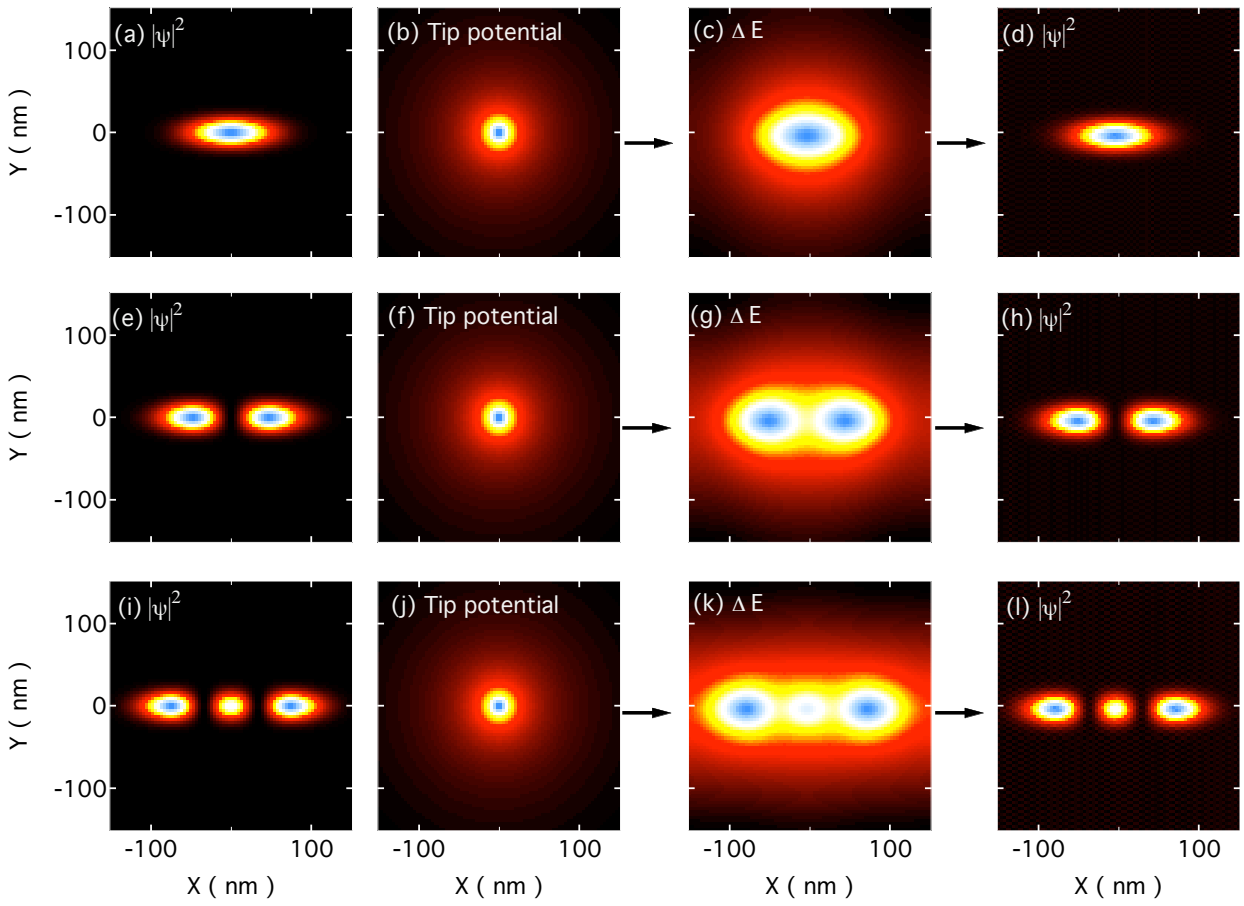

Figure 4.14: First column: Plots of the amplitude squared of the wavefunction for (a) the (0,0) ground state, (e) the (1,0) excited state and (i) the (2,0) excited state. Second column: Plot of tip perturbation calculated using a charged sphere model for the tip with $H_{tip} = 10$ nm and $V_{tip} = -10$ mV. Third column: Plot of the shift in the energy of the state depicted in the first column as a function of tip position as the charged tip is scanned above the quantum dot. Here ΔE is given by the convolution of the wavefunction squared and the tip perturbation plotted in the first and second columns. Fourth column: Results of the deconvolution of ΔE (third column) with respect to the tip perturbation (second column) to extract the wavefunction amplitude. The deconvolution process is performed by dividing the Fourier transform of ΔE by the Fourier transform of the tip perturbation and taking the inverse Fourier transform of the result to obtain the amplitude square of the wavefunction. The wavefunction amplitudes of all the states shown here are reconstructed accurately, demonstrating our proposed technique for extracting the wavefunction.

What is referred to as resolution here is loosely defined as the accuracy with which extracting the wavefunction is possible. There are three major parameters that determine if the imaging resolution is sufficient for extracting the wavefunction. These three parameters are (1) the ratio of the width of the tip potential to that of the wavefunction, (2) the measurement noise and (3) the accuracy with which the tip potential in known. Lower temperatures can also improve the imaging resolution, however it has a less significant effect on the resolution.

Relative width of tip perturbation to the wavefunction As common sense suggests the smaller the tip potential relative to the size of the wavefunction the better the resolution. If the size of the tip perturbation is very small, e.g. a delta function, the convolution of the tip perturbation and $|\psi|^2$ is very close to $|\psi|^2$, and ΔE is almost a direct measure of $|\psi|^2$. On the other hand if the tip perturbation is much larger than $|\psi|^2$ then ΔE is almost a direct measure of the tip perturbation and contains very little information about the wavefunction. When the two sizes are comparable then the resolution becomes much more sensitive to the other factors, i.e. noise and the accuracy with which the tip perturbation is known. Remember that the deconvolution process can be performed by taking the Fourier transform of ΔE divided by the Fourier transform of the tip potential $\phi_{tip}(\vec{r})$ in order to get the Fourier transform of $|\psi|^2$. If $|\psi|^2$ is smaller than $\phi_{tip}(\vec{r})$ then in k-space it will be larger, so that in the deconvolution process something large is divided by something small to calculate something large, which is an unstable process. So in general we need to have a tip perturbation that is smaller than the wavefunction. The smaller the tip perturbation, the more accurate the wavefunction extraction.

The relative size of tip perturbation $\phi_{tip}(\vec{r})$ to wavefunction can be reduced by either narrowing $\phi_{tip}(\vec{r})$ or by choosing systems with wavefunctions spread over larger areas. In our simple model of the tip as a charged metallic sphere held at H_{tip} above the quantum dot the tip potential is given by:

$$\phi_{tip}(\vec{r}) = \frac{2R_{tip}V_{tip}}{(\epsilon_0 + \epsilon_1)(r^2 + H_{tip}^2)^{1/2}} \tag{4.9}$$

where R_{tip} is the tip radius and ϵ_1 is the dielectric constant of the semi-conductor heterostructure that contains the dot. The FWHM of the tip potential in this model is proportional to H_{tip}, and can be reduced by imaging with the tip closer to the surface. In quantum dots formed in 2DEGs that are buried in semi-conductor heterostructures, such as the quantum dot imaged in the previous chapter, the quantum dot is always formed underneath the surface at a depth of between 30 to 300 nms. This places a limit on how close the tip can get to the quantum dot, hence placing a limit on the imaging resolution. In this model the radius of the tip R_{tip} or the tip voltage V_{tip} do not affect the FWHM of the tip potential. Higher resolution can therefore be achieved when imaging systems where electrons are trapped closer to the surface, e.g. in a nanowire or 2DEGs formed on the surface.

Imaging systems with broader wavefunctions is another way of imaging with enhanced resolution. As shown previously an elongated quantum dot can be imaged with slightly higher resolution in the direction of lower confinement compared to a symmetric quantum dot with higher confinement. A number of systems can be thought of for this purpose, e.g. larger quantum dots, elongated quantum dots formed in nanowires or in 2DEGs, doubled quantum dots, all of which have wavefunctions that are spread over a larger area and can be imaged using this technique. One should

note that although the larger wavefunction can be imaged more easily, features in the wavefunction that are smaller than the tip perturbation will still be hard to image. Furthermore, these systems can only be imaged if they show Coulomb blockade. Making quantum dots larger can cause problems for detection of the Coulomb blockade signal in the few-electron regime. This is due to the fact that coupling to the leads becomes very small if the puddle of few-electrons is formed far from the tunneling barriers, which leads to weaker Coulomb blockade peaks that can be hard to detect. For much larger quantum dots with larger total capacitance C, lower temperatures are also needed to keep k_BT smaller than the charging energy $E_C = e^2/C$, a requirement for observing Coulomb blockade.

Noise in conductance measurements As discussed previously noise in conductance measurements affects the resolution since it determines the accuracy with which ΔE is measured. In the regime where the size of the tip potential is of the same order as the size of $|\psi|^2$ noise becomes more important since each data point in the plot of ΔE as a function of $\vec{r}_{tip}$ contains as much information about the tip perturbation as it has about $|\psi|^2$, and therefore noise would affect the accuracy with which $|\psi|^2$ is known to a more degree.

Shape of tip perturbation The accuracy with which the tip potential ϕ_{tip} is known plays an obvious role in determining the imaging resolution. The deconvoution is done with respect to ϕ_{tip}. If the tip potential assumed in the deconvolution process is different from the real value of ϕ_{tip} the outcome of the deconvolution $|\psi|^2$ will also be different from the real value. Again if the tip perturbation is much smaller in

width than $|\psi|^2$ the sensitivity to its exact shape is lower, however if the sizes of the tip perturbation and $|\psi|^2$ are close knowing the exact shape of the tip perturbation becomes crucial.

The shape of the tip perturbation can be measured or modeled. In this chapter we have adopted a simple model for the tip as a charged sphere. More accurate modeling of the shape of the perturbation in the electron gas induced by the tip is not easy due to screening effects of the metallic surface gates and of the 2DEG in the leads. The accurate shape of the SPM tip is also not known. Although the SPM tips are perfectly cone shaped when purchased, with an accurately known radius of curvature, by the time Coulomb blockade imaging is performed their shape could be changed. This change is due to evaporation of metal on the tips to make them conductive and also due to topographical imaging using the same SPM tips. When purchased the SPM tips do not conduct, therefore a thin layer of Cr is evaporated on the tips in order to make them conductive. This evaporation can cause the tip to loose its symmetric shape or if not done well might cause only parts of the tip to conduct. Furthermore, in order to locate the quantum dot device, topographical imaging is done prior to Coulomb blockade imaging, where the SPM tip is dragged along the surface and might have parts chipped off or might pick up junk from the surface. All of this affects the shape of the tip potential at the quantum dot.

Temperature The non-linear dependence of the dot conductance to the energy levels inside the quantum dot in the Coulomb blockade regime is at the center of our imaging technique, allowing us to measure the energy levels with high accuracy. This non-linearity is enhanced as the temperature is decreased through the narrowing of the

temperature broadened Coulomb blockade peaks. The maximum conductance, G_{max}, has a $\frac{1}{k_B T}$ dependence and increases with temperature enhancing the signal to noise ratio in the conductance images. Through the above phenomena lower temperature contributes to higher imaging resolution in this technique.

4.5 Experimental results

In the experiment described in chapter 3 we have imaged the last electron on a quantum dot. From the images we extracted a map of ΔE as a function of tip position (figure 3.3), i.e. step 1 towards extracting the wavefunction. The results of the deconvolution of $\Delta E(\vec{r}_{tip})$ with respect to the tip perturbation, i.e. step 2, show features that might be associated with the wavefunction, however accurate extraction of the wavefunction was not possible due to resolution limitation discussed below.

The width of the wavefunction of the one-electron ground state in the quantum dot can be estimated from the energy level spacing $\hbar\omega$ assuming the dot has a symmetric harmonic potential. The energy level spacing read from plots of differential conductance as a function of $V_{side-gate}$ and V_{SD} shown in figure 3.2 is $\hbar\omega = 3.1$ meV. The one-electron ground state in this harmonic potential has a FWHM of 45 nm. The FWHM of the tip perturbation was of the order of 200 nm, much larger than the wavefunction. Given these parameters and the previous resolution discussion it is obvious that extracting the wavefunction is very difficult.

Figure 4.15 plots the results of the deconvolution of $\Delta E(\vec{r}_{tip})$ with respect to a tip perturbation calculated using our simple charged sphere model with $H_{tip} = 152$ nm (for a tip 100nm above the surface and a 2DEG 52nm below the surface) and

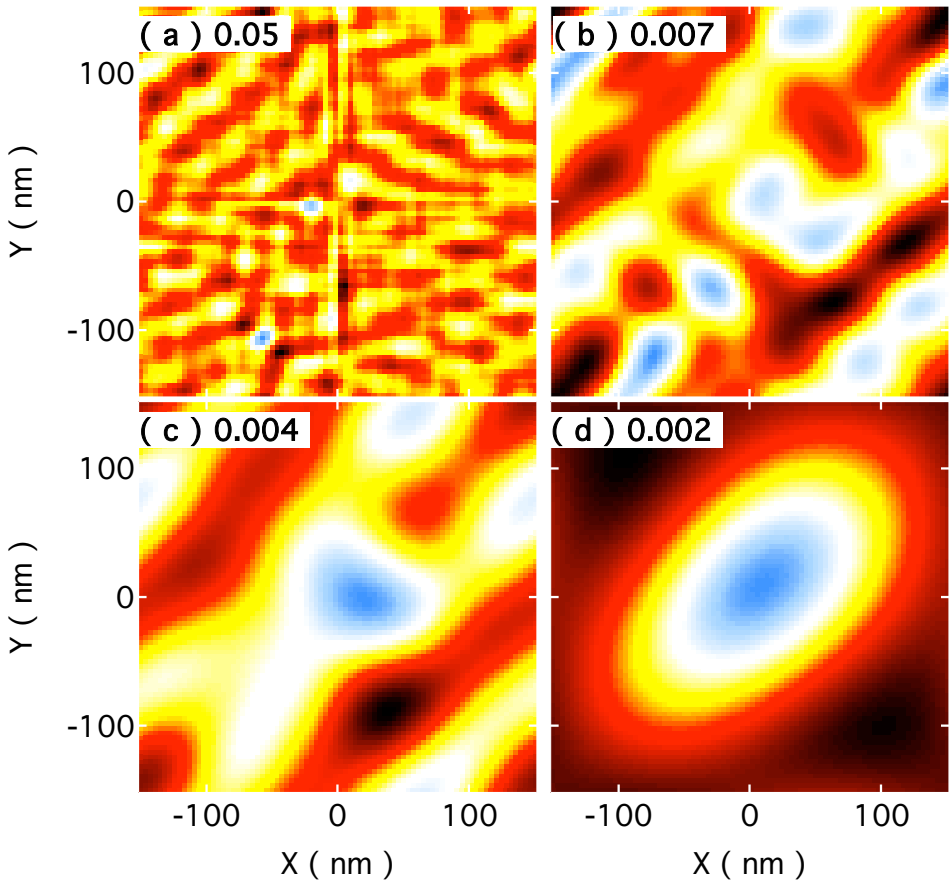

Figure 4.15: Result of the deconvolution of $\Delta E(\vec{r}_{tip})$ with respect to tip perturbation. The tip perturbation is calculated assuming a simple charged sphere model for the tip, with $H_{tip} = 152$ nm and $V_{tip} = -90$ mV. A gaussian filter of the form $e^{-k^2/2\alpha}$ is applied in k-space at the last stage before the inverse Fourier transform is taken. The values of α are indicated on the plots in units of nm^{-2}. As the filtering has increased from (a) to (d) the high-frequency features disappear. In the intermediate filtering regime, (b) & (c) semi-stable features of similar size scales to the wavefunction appear, however in this regime it is not possible to prove that these features correspond to the wavefunction.

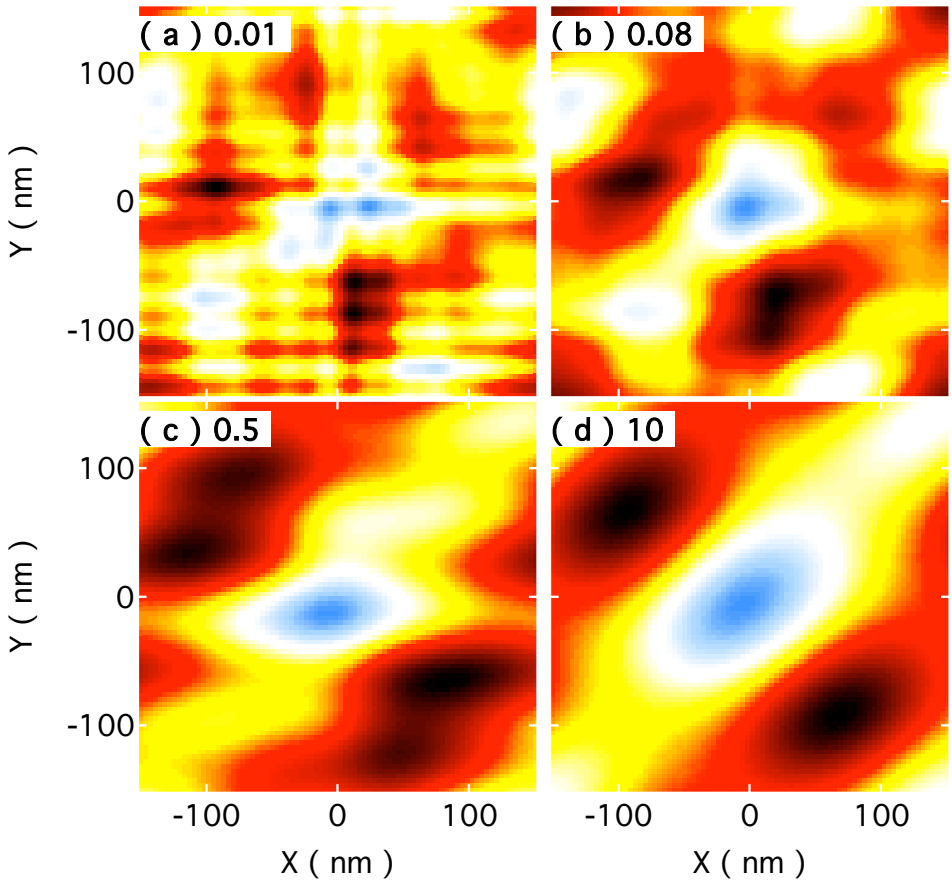

Figure 4.16: Result of the deconvolution of $\Delta E(\vec{r}_{tip})$ with respect to tip perturbation. The tip perturbation is calculated assuming a simple charged sphere model for the tip, with $H_{tip} = 152$ nm and $V_{tip} = -90$ mV. A different filtering mechanism than that of figure 4.15 is used here. The filter is applied in k-space at the last stage before the inverse Fourier transform is taken and is zero for all $\vec{r}_{tip}$ at which the Fourier transform of the tip perturbation is less than a cut-off value and one for all other $\vec{r}_{tip}$. The cut-off values are indicated in the plots in units of mV. Similar trends as seen in figure 4.15 are observed here, however the deconvoution results are different demonstrating the importance of the filtering mechanism. In plot (d) too much filtering is applied, resulting in a feature much larger than the expected wavefunction.

$V_{tip} = -90$ mV. A necessary part of the deconvolution process is filtering in k-space. The filtering is done at the last stage before taking the inverse Fourier transform to obtain the wavefunction. In the plots shown in figure 4.15 a gaussian filter is used that multiplies the k-space by $e^{-k^2/2\alpha}$, where α is a tunable parameter indicated in white on the plots in figure 4.15. In figure 4.15a the filtering is not sufficient to eliminate the high-frequency numerical artifacts of the boundaries or the high-frequency noise. As more filtering is applied the high-frequency features disappear as expected, however we start to loose frequency components of the wavefunction itself. In figures 4.15b and c features on the same size scale as the wavefunction appear in the deconvolution plots. These features are stable throughout a range of values for α suggesting that they might indeed be features corresponding to the wavefunction and not artificially produced as a result of filtering. Finally in figure 4.15d too much filtering is applied and the deconvolution results in a feature much larger than that expected for the wavefunction.

To compare the effects of different filtering mechanisms in the deconvolution process a second filtering technique was applied in the deconvolution of $\Delta E(\vec{r}_{tip})$ with respect to the tip perturbation. Figure 4.16 plots the results of this deconvolution. Here a mask is applied to the k-space before taking inverse Fourier transform which is one for all $\vec{r}_{tip}$ except for those $\vec{r}_{tip}$ at which the Fourier transform of the tip perturbation is less than a cut-off value, where it is zero. Applying this mask prevents the noise existing in the Fourier transform of ΔE to be amplified when divided by small values in the Fourier transform of the tip perturbation. The cut-off values are indicated on the plots in figure 4.16. A similar trend to that of figure 4.15 is observed here, however

the convolution results are different. In the intermediate filtering region (figure 4.16 b & c) a stable feature appears that could again correspond to the wavefunction. Better filtering mechanisms such as the optimal filtering for deconvolution described in [44] could potentially be used, however we expect no major changes in the deconvolution results here, given the sizes of the wavefunction and the tip perturbation.

Chapter 5

Imaging few-electron quantum dots in a magnetic field

5.1 Introduction

Understanding the behavior of electrons and spins inside few-electron quantum dots are subject of great interest. In a proposal by Loss and DiVincenzo [15] an array of one-electron quantum dots is suggested as a building block for a quantum computer, where the electron spin on the quantum dot is proposed as a qubit and tunneling is used to entangle spins on adjacent dots. One-electron quantum dots were developed in single [2, 6, 14, 7], double [8, 10] and triple [45] dot circuits. In the Loss-DiVincenzo proposal single and double qubit operations are performed using local magnetic fields that couple to the spin of the electron on a single quantum dot or on double dots. Understanding the interaction of electrons with the magnetic field is therefore essential to advancements in solid-state quantum information processing.

Furthermore quantum dots show atomic-like behavior and are referred to as artificial atoms . The atomic like shell structure of electrons in quantum dots in the presence of a magnetic field reflects the interesting similarities as well as differences between quantum dots and real atoms [2, 6, 14, 7], further motivating a study of quantum dots in a magnetic field.

Scanning probe microscopy (SPM) is a powerful tool for studying mesoscopic systems. Various SPM techniques have been developed and used to measure and manipulate electrons and spins at low temperatures. Images of coherent electron flow from a quantum point contact (QPC) in a 2DEG were obtained using a liquid-He temperature SPM [22, 23, 21] and cyclotron orbits were imaged in a magnetic field [46]. In the quantum Hall regime electrons inside a 2DEG were imaged, and localized states as well as edge states were observed [24, 25, 26, 27, 28]. Recently a magnetic resonance force microscope (MRFM) was used to image an individual unpaired spin in Silicon dioxide [34]. We have previously imaged electrons in a one-electron quantum dot in the Coulomb blockade regime, using a liquid-He temperature SPM [47]. In this chapter we describe SPM imaging of a one-electron quantum dot in a strong magnetic field and demonstrate how the images can be used as a measure of the diamagnetic energy shift of the energy levels inside the quantum dots.

5.2 Experimental Setup

The imaging technique, shown in figure 5.1, is similar to that of chapter 3 with the addition of a perpendicular magnetic field. A charged SPM tip is scanned at a fixed hight above the surface of the quantum dot. The tip capacitively couples

to the quantum dot, changing the potential landscape forming the quantum dot as it is scanned above it. The energy levels inside the quantum dot shift up or down depending on the tip voltage. The images are obtained by recording the conductance through the quantum dot in the Coulomb blockade regime as a function of tip position.

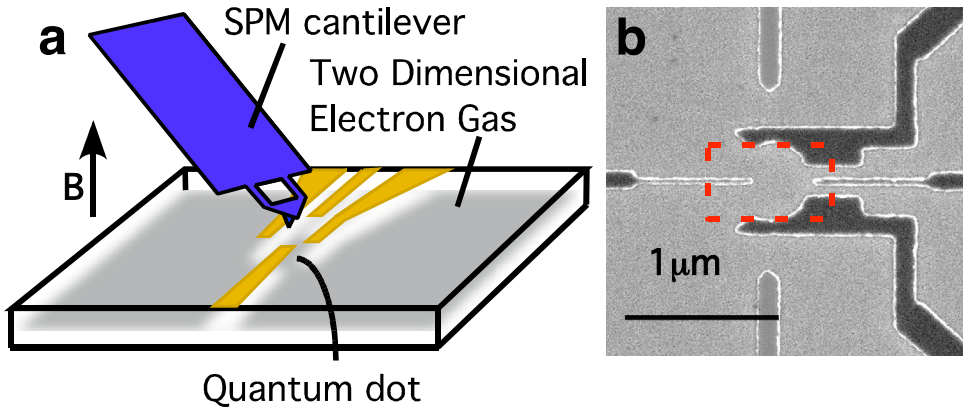

Figure 5.1: (a) Experimental Setup. A positively charges SPM tip is scanned at a fixed height above the surface of a heterostructure forming that contains a quantum dot. The SPM and the quantum dot device are mounted in a He-4 cryostat and cooled to 1.7K. Images are obtained by recording the conductance through the quantum dot as a function of tip position. (b) A scanning electron micrograph of the quantum dot, formed by Ti surface gates on GaAs/AlGaAs heterostructure. Only the gates in the darker shade have been energized for this experiment. The dashed line indicates the area covered by the conductance images.

The quantum dot (Figure 5.1b) is formed in a GaAs/$Al_{0.3}Ga_{0.7}As$ heterostructure by Ti surface gates. The heterostructure contains a 2DEG with measured density $3.7 \times 10^{11} cm^{-2}$, and mobility 480,000 cm^2 V^{-1} s^{-1} at 4.2 K. The heterostructure was grown by molecular beam epitaxy with the following layers: 5 nm GaAs cap layer, 20 nm $Al_{0.3}Ga_{0.7}As$, Si delta doping layer, 22 nm $Al_{0.3}Ga_{0.7}As$, 1000 nm GaAs, a 20 period GaAs/$Al_{0.3}Ga_{0.7}As$ supper lattice, 100 nm GaAs buffer, and a semi-insulating GaAs substrate. The 2DEG is formed at the interface between the $Al_{0.3}Ga_{0.7}As$ and the GaAs layers 47 nm below the surface. The sample was mounted in a liquid-He

cooled SPM and cooled to 1.7 K.

The quantum dot is tuned in the Coulomb blockade resonant tunneling regime where conductance occurs through only a single state inside the quantum dot and the conductance peaks are thermally broadened. Figures 5.2 shows plots of differential conductance through the quantum dot as a function of $V_{side-gate}$ and source to drain voltage V_{SD} at B = 0 T and B = 3 T. The number of electrons on the dot is one inside the diamond shaped area of low conductance and zero for more negative values of V_{SD} as shown in figures 5.2a and b. Two lines associated with tunneling through the one-electron ground state and the first excited state are indicated in white and yellow respectively. The energy separation Δ between these two states is equal to the V_{SD} at which these two lines meet. From figures 5.2a and b we obtain $\Delta = 2.7 \pm 0.15$ meV at B = 0 T and $\Delta = 1.7 \pm 0.15$ meV at B = 3 T.

5.3 Experimental Results

Figure 5.3a shows an image of the last electron on the quantum dot, obtained at $V_{SD} = 0$. The voltage applied between the tip and the 2DEG, V_{tip}, is -50 mV, however the tip acts as a positive tip adding electrons to the dot when it is brought close to the quantum dot. This can be due to the contact potential between tip and the quantum dot, which is the effective potential difference between the two when both are grounded due to the difference in work functions. The image is a plot of dot conductance vs tip position and shows a ring of high conductance centered around the quantum dot. When the tip is inside the ring the dot contains one electron and when the tip is moved outside the ring the last electron on the quantum dot is pulled out.

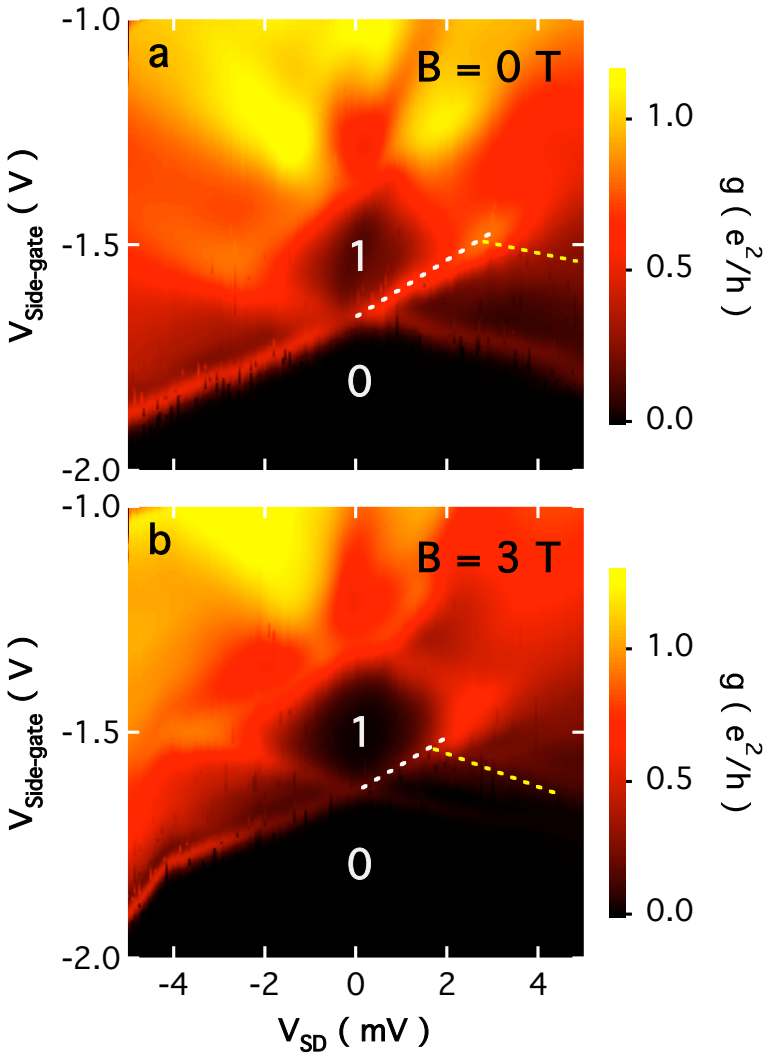

Figure 5.2: Plots of differential conductance $g = dI/dV_{SD}$ as a function of $V_{side-gate}$ and source-to-drain voltage V_{SD} at T = 1.7 K with a perpendicular magnetic field (a) B = 0 T and (b) B = 3 T. The number of electrons on the dot is indicated. The white/yellow dashed lines point out a feature associated with tunneling through the one-electron ground/excited state. The energy spacing between these two states Δ is equal to the source to drain voltage at which the two lines meet. From these two plots we obtain $\Delta = 2.7 \pm 0.15$ meV at B = 0 T and $\Delta = 1.7 \pm 0.15$ meV at B = 3 T.

The ring is formed by a Coulomb blockade peak at the degeneracy point where the dot can hold either zero or one electrons. This ring is therefore a contour of constant tip to dot coupling at which the one-electron ground state in the dot is in resonance with the Fermi energy of the leads.

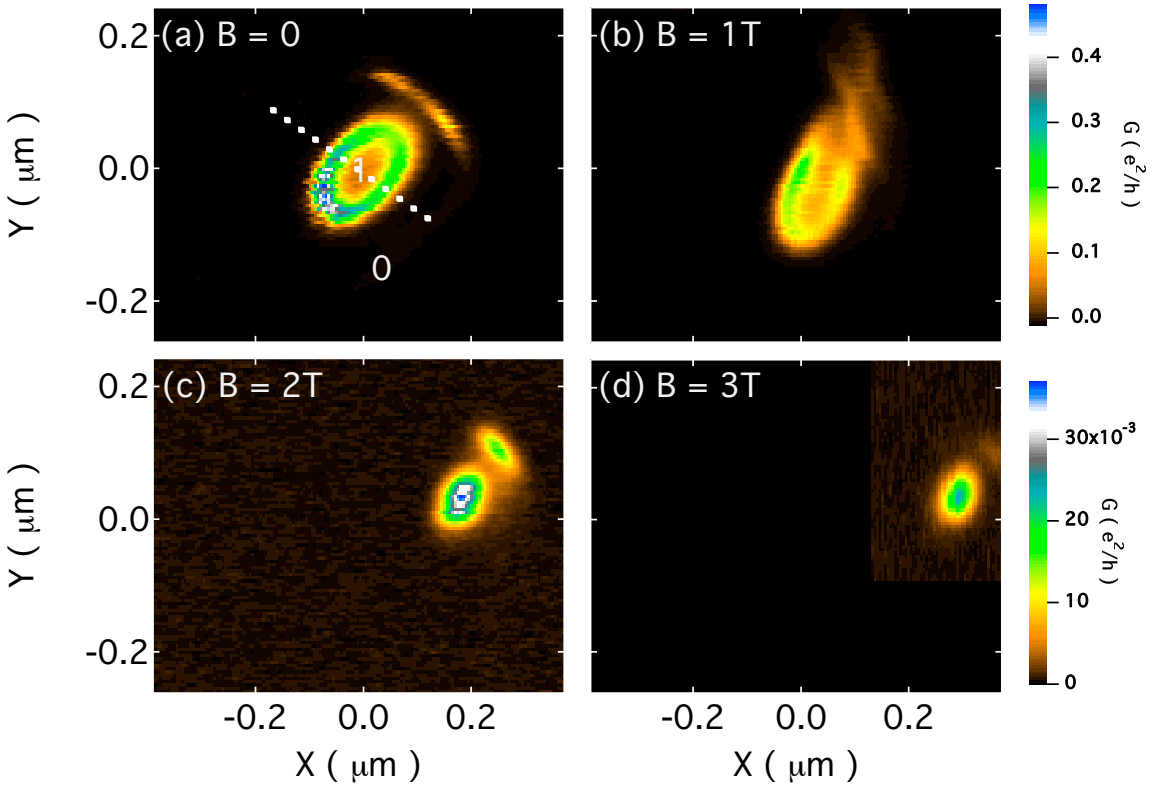

Figure 5.3: (a-d) Coulomb blockade images of a single-electron quantum dot at T = 1.7 K, showing the dot conductance G versus tip position. The images are obtained in a perpendicular magnetic field of 1, 2, 3 and 4 Telsa for a-d. The ring of high conductance centered around the dot is formed by the Coulomb blockade peak between 0 and 1 electron in the dot. As the magnetic field is increased the diameter of the ring reduces due to a diamagnetic energy shift in the quantum dot.

As the magnetic field is increased from 0 to 3 Tesla the ring observed in the image of the last electron shrinks and changes shape (Figures 5.3a-d). The change in ring diameter indicates a change in the energy level inside the quantum dot as described

in the previous chapters. In a perpendicular magnetic field, energy levels inside the quantum dot shift up or down depending on their angular quantum number. This diamagnetic energy shift is due to the additional magnetic confinement that competes with the electrostatic dot confinement in determining the energy levels. Here we show that the shrinking of the ring diameter is consistent with the expected diamagnetic shift, estimated independently from differential conductance measurements performed on the quantum dot.

The diamagnetic shift associated with the one-electron ground state energy level in the quantum dot can be estimated by assuming a general elongated harmonic potential for the quantum dot with resonant frequencies ω_1 and ω_2. In a noninteracting electron picture the one-electron energy levels associated with a harmonic potential in a perpendicular magnetic field are given by [48]

$$E_{n,m}(B) = (n+1)\frac{\hbar}{2}\sqrt{(\omega_1+\omega_2)^2+\omega_c^2} + m\frac{\hbar}{2}\sqrt{(\omega_1-\omega_2)^2+\omega_c^2} \tag{5.1}$$

where n and m are the radial and angular quantum numbers, and ω_c is the cyclotron frequency given by eB/m^*.

From equation 5.1 the diamagnetic shift of the one-electron ground state is given by:

$$E_{0,0}(B=3T) - E_{0,0}(B=0) = \frac{\hbar}{2}\sqrt{(\omega_1+\omega_2)^2+\omega_c(B=3T)^2} - \frac{\hbar}{2}(\omega_1+\omega_2) \tag{5.2}$$

where in GaAs, ω_c is 1.76 meV per Tesla and 5.28 meV at 3 Tesla.

The resonant frequencies ω_1 and ω_2 are given by the energy separation between the ground state and first excited state Δ. As explained previously Δ can be read from a plot of differential conductance as a function of $V_{side-gate}$ and V_{SD} (Figure 5.2a

and b). Figure 5.4 shows Δ obtained from differential conductance measurements at different magnetic fields. From equation 5.1 we expect Δ to depend on magnetic field in the following way:

$$\Delta = E_{1,-1} - E_{0,0} = \frac{\hbar}{2}(\sqrt{(\omega_1 + \omega_2)^2 + \omega_c^2} - \sqrt{(\omega_1 - \omega_2)^2 + \omega_c^2}) \tag{5.3}$$

where $\omega_c = eB/m^*$.

Fitting equation 5.3 to the data points on graph 5.4 gives $\hbar\omega_1 = 2.7 \pm 0.13$ meV and $\hbar\omega_2 = 5.2 \pm 0.8$ meV (blue line on figure 5.4). The value of the diamagnetic shift can be calculated by inserting these values for ω_1 and ω_2 into equation 5.2. The calculated diamagnetic shift at B = 3 T is 0.80 ± 0.10 meV.

The diamagnetic shift of the ground state energy levels inside the quantum dot causes the ring in the conductance images shown in figure 5.3 to shrink. Weather the ring shrinks or expands as a result of a change in the energy level inside the quantum dot depends on the tip voltage V_{tip}. For an effectively positive V_{tip}, such as V_{tip} for the images in figure 5.3, a positive shift in an energy level, caused for example by the diamagnetic shift, moves the tip position at which the dot is in resonance with the dot closer to the dot causing the rings to shrink. However for an effectively negative V_{tip}, a negative shift in the dot energy levels, caused by making $V_{side-gate}$ less negative, also causes the rings to shrink.

The amount by which the diameter of the ring seen in the conductance images of figure 5.3 shrinks is a measure of the energy shift in the ground state energy level of the quantum dot. If the capacitance coupling between the tip and the dot is known, the diamagnetic shift of the ground state energy level can be extracted from figure 5.3. Here we assume a very simple model for the tip to dot coupling which assumes that

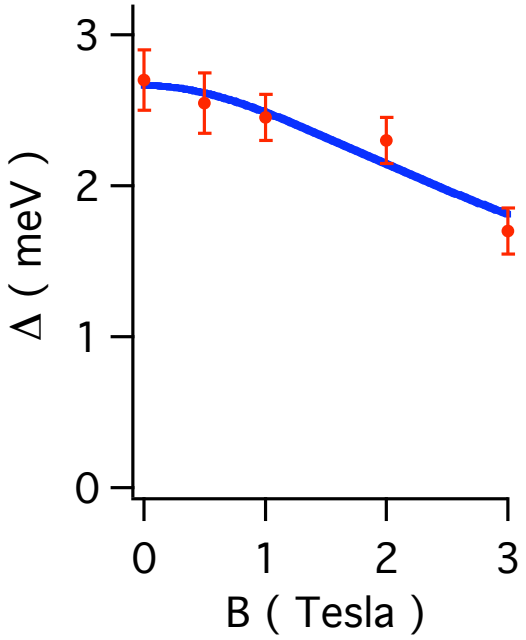

Figure 5.4: Plot of energy level separation Δ between the one-electron ground state and the first excited state as a function of magnetic field. Each data point is obtained from a plot of differential conductance through the dot as a function of $V_{side-gate}$ and V_{SD} at the corresponding perpendicular magnetic field. The blue solid line is a fit to the data points of the expected form of Δ given in equation 5.3. From this fit we obtain the following values for ω_1 and ω_2 resonance frequencies: $\hbar\omega_1 = 2.7 \pm 0.13$ meV and $\hbar\omega_2 = 5.2 \pm 0.8$ meV.

the dot energy changes linearly with r_{tip} and is given by

$$\Delta E = C\ \Delta r_{tip} \tag{5.4}$$

where C is a constant whose value depends on V_{tip} and H_{tip}. Adopting this model although not accurate is acceptable since the tip potential is much broader than the ground state wavefunction in the quantum dot, and effectively shifts the dot potential up or down as the tip is scanned without perturbing it. Therefore over small ranges of tip position we can assume that the shift in the dot potential is linear with the tip position.

The constant C in equation 5.4 can be estimated using the temperature broadened width of the Coulomb blockade peaks forming the rings. Figure 5.5 shows the cross sections of the four rings shown in Figure 5.3 along the indicated white dashed line, each showing two Coulomb blockade peaks. The dot is tuned in the resonant tunneling regime where the Coulomb blockade peaks are temperature broadened. The FWHM of a Coulomb blockade peak in this regime in given by $3.5k_BT$. We have measured the temperature of electrons from the width of Coulomb blockade peaks in a plot of conductance vs $V_{side-gate}$ without the tip present to be 1.8 K, making the FWHM of the Coulomb blockade peak 0.54 meV. The dashed line on figure 5.5 is a fit to the peaks shown in red of the temperature broadened Coulomb blockade peak line-shape. The FWHM of the peaks measured from this fit is 37 nm in tip position. This indicates that a change in the tip position of 37 nm causes a change in the dot energy equal to 0.54 meV. Therefore the constant C in equation 5.4 is given by $C = 0.54/37 = 0.0145$ meV/nm.

Finally we can compare the independently estimated value for the diamagnetic

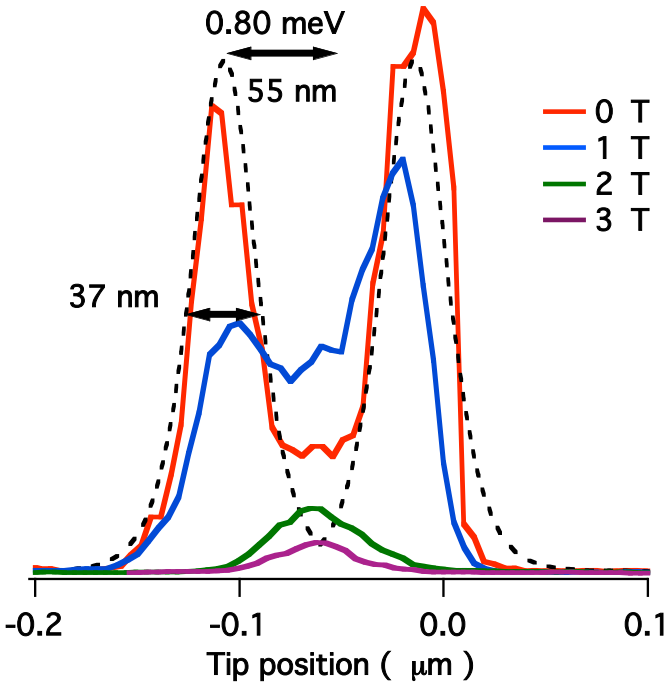

Figure 5.5: Cross section of the Coulomb blockade rings from figure 5.3 are plotted along the white dashed line. The magnetic field value for each trace is shown on the right. Each trace shows two Coulomb blockade peaks. As the magnetic field is increased, the ring shrinks and the two peaks move towards each other. The temperature broadened width of the peak at zero magnetic field can be used to convert shifts in tip position to shifts in dot energy, assuming the dot energy changes linearly with tip position. The dashed line is a fit to the trace shown in red of a temperature broadened Coulomb blockade peak line-shape. The FWHM of the peak given by this fit is 37 nm in tip position and corresponds to a $3 \times k_B T = 0.54$ meV energy change. The diamagnetic shift at 3 Tesla estimated from independent conductance measurements is 0.80 meV, associated with a shift of 55 nm in tip position, as shown above. We therefore expect the peaks to move inwards by 55 nm at 3 Tesla, causing them to merge together and form a single peak, as observed in the plot above.

shift with the change in the ring diameter observed in figure 5.3. Using the above value for C we expect the 0.80 meV estimated diamagnetic shift to cause a 55 nm shift in peak position. The shift is shown by the black arrow on figure 5.5. A 55nm shift would cause the two peaks to merge together and form one peak. This is exactly what is observed in the images, demonstrating that the shift in the peak positions is consistent with the estimates diamagnetic shift. Note that in the last two traces in figure 5.5, obtained at B = 2 T and B = 3 T, where the two peaks have merged together, the exact position of the peaks is not known, since both the position and the amplitude of the rings change. We conclude that the reduction in the ring diameter in a magnetic field is mainly due to a diamagnetic shift in the ground state energy of the dot, and can be used as a measure of this energy shift.

Figures 5.3 and 5.5 show a reduction in the peak amplitude as the magnetic field is increased. The amplitude of a Coulomb blockade peak in the resonant tunneling regime is given by $G_{max} = \frac{e^2}{4k_BT}\Gamma$, where Γ is the tunneling rate through the quantum dot tunneling barriers. As the magnetic field is increased the wavefunction of electrons inside the quantum dots shrinks due to the increased magnetic confinement. This reduces the overlap of the electron wavefunction inside the quantum dot and the electrons in the leads, causing a reduction in the tunneling rate Γ which reduces the Coulomb blockade peak amplitude. The reduction in peak amplitude places a limit on the range of magnetic fields for which a conductance ring associated with a particular level can be studies at fixed V_{tip} and $V_{side-gate}$ before the peak is buried in noise.

Furthermore, figure 5.3 shows changes in the shape of the ring as the field is increased. The shape of the ring in the conductance images is given by the shape of

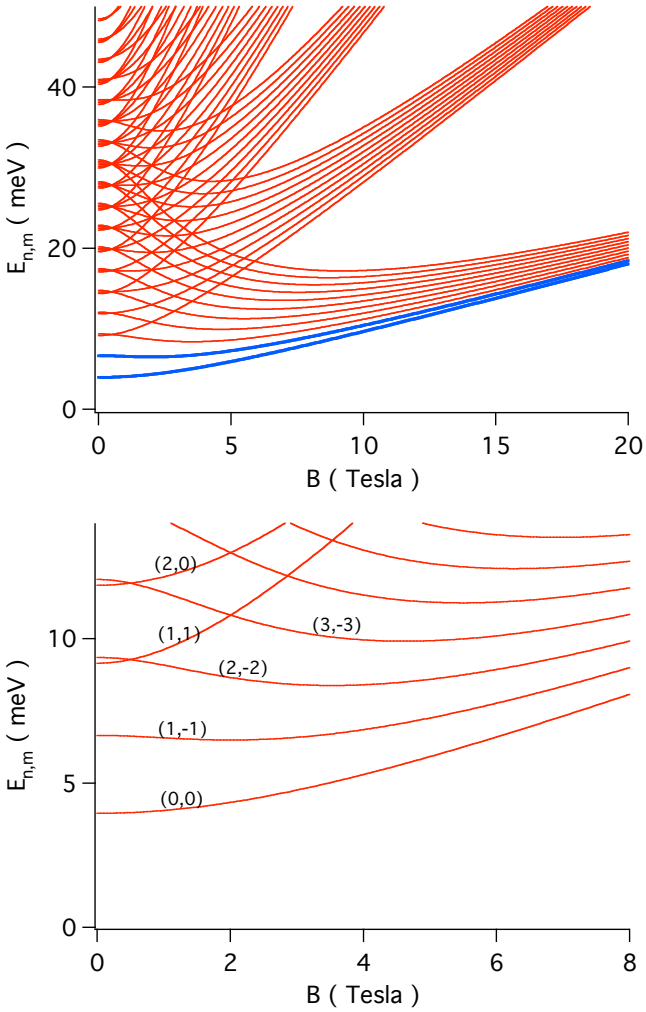

Figure 5.6: (a) Eigen energies of an elongated two dimensional harmonic potential with resonant frequencies ω_1 and ω_2 in a perpendicular magnetic field B, calculated using equation 5.1. The values of the resonant frequencies are $\hbar\omega_1 = 2.7$ meV and $\hbar\omega_2 = 5.2$ meV, matching the resonant frequencies of the quantum dot discussed here. The eigen energies change in B due to the additional confinement of the magnetic field. At large values of B, when the magnetic confinement dominates, Landau levels are formed. The difference between the two energy levels shown in blue decreases with B, consistent with our measurements of Δ in this chapter. (b) Zoom-in on the low B values on plot a. While for one or two electrons the ground state remains the same as B is changed, for more electrons there are transitions in the ground state as energy levels cross. These transitions can be probed using our SPM technique.

the tip potential convoluted with the squared amplitude of the electronic wavefuntion in the quantum dot, as described in chapter 4. The change in the ring shape can therefore be due to changes in the tip potential or to changes of the wavefunction. Although the magnetic field does not affect the tip potential, as the tip is moved above the quantum dot, changes in the screening of the tip potential by the fixed surface gates or by the 2DEG may cause variations in the tip potential. This effect is specially important when the scan range is large compared to the lithographic size of the quantum dot, i.e. where the gates are positioned. It is therefore preferable to image in smaller areas within the gates of the quantum dot.

A more interesting cause for the changes in the shape of a Coulomb blockade ring can be changes in the wavefunction of electrons inside the quantum dot. In the images shown in figure 5.3 conductance occurs through the one electron ground state with quantum numbers (n,m) = (0,0). Figure 5.6 plots the eigen energies of an elongated two dimensional harmonic potential with resonant frequencies ω_1 and ω_2, where $\hbar\omega_1 = 2.7$ meV and $\hbar\omega_2 = 5.2$ meV, matching the resonant frequencies of our quantum dot. These energies are given by equation 5.1. The (0,0) state remains the ground state as the magnetic field is increased. However, when the dot contains 3 or more electrons the magnetic field causes transitions in the ground state as different energy levels cross. These sudden transitions of the wavefunction can be detected through a sudden change in the shape of the ring. This imaging technique, with an improved resolution, can be used to probe orbital transitions in the quantum dot by careful monitoring of the shape of the rings as the magnetic field is changed.

Bibliography

[1] L. P. Kouwenhoven, C. M. Marcus, P. L. McEuen, S. Tarucha, R. M. Westervelt, and N. S. Wingreen, *Electron Transport in Quantum Dots*, NATO ASI conference proceedings, edited by L. L. Sohn, L. P. Kouwenhoven and G. Schön, (Kluwer, Dordrecht 1997).

[2] L. P. Kouwenhoven, D. G. Austing, and S. Tarucha, *Few-Electron Quantum Dots*, Rep. Prog. Phys. **64**, 701 (2001).

[3] C. W. J. Beenakker, *Theory of Coulomb Blockade Oscillations in the Conductance of a Quantum Dot*, Phys. Rev. B **44**, 1646 (1991).

[4] J. h. F. Scott-Thomas, S. B. Field, M. A. Kastner, H. I. Smith, and D. A. Antoniadis, *Conductance Oscillations Periodic in the Density of a One-Dimensional Electron Gas*, Phys. Rev. Lett. **62**, 583 (1989).

[5] M. A. Kastner, *The Single-Electron Transistor*, Rev. Mod. Phys. **64**, 849 (1992).

[6] S. Tarucha, D. G. Austing, T. Honda, R. J. van der Hage, and L. P. Kouwenhoven, *Shell Filling and Spin Effects in a Few Electron Quantum Dot*, Phys. Rev. Lett. **77**, 3613 (1996).

[7] M. Ciorga, A. S. Sachrajda, P. Hawrylak, C. Gould, P. Zawadzki, S. Jullian, Y. Feng, and Z. Wasilewski, *Addition Spectrom of a Lateral Dot from Coulomb Blockade and Spin-Blockade Spectroscopy*, Phys. Rev. B **61**, R16315 (2000).

[8] J. M. Elzerman, R. Hanson, J. S. Greidanus, L. H. Willems van Beveren, S. De Franceschi, L. M. K. Vandersypen, S. Tarucha, and L. P. Kouwenhoven, *Few-Electron Quantum Dot Circuit with Integrated Charge Read Out*, Phys. Rev. B **67**, R161308 (2003).

[9] R. M. Potok, J. A. Folk, C. M. Marcus, V. Umansky, M. P. Hanson, and A. C. Gossard, *Spin Polarized Current from Coulomb Blockaded Quantum Dots*, Phys. Rev. Lett. **91**, 16802 (2003).

[10] I. H. Chan, P. Fallahi, A. Vidan, R. M. Westervelt, M. Hanson, and A. C. Gossard, *Few-electron double quantum dots*, Nanotech. **15**, 609 (2004).

[11] D. M. Zumbühl, C. M. Marcus, M. P. Hanson, and A. C. Gossard, *Cotunneling Spectroscopy in Few-Electron Quantum Dots*, Phys. Rev. Lett. **93**, 256801 (2004).

[12] A. K. Hüttel, S. Ludwig, H. Lorenz, K. Eberl, and J. P. Kotthaus, *Direct control of the tunnel splitting in a one-electron double quantum dot*, Phys. Rev. B **72**, 081310 (2005).

[13] M. A. Kastner, *Artificial Atoms*, Phys. Today **Jan**, 24 (1993).

[14] R. C. Ashoori, *Electrons in Artificial Atoms*, Nature **379**, 413 (1996).

[15] D. Loss and D. P. DiVincenzo, *Quantum Computation with Quantum Dots*, Phys. Rev. A **57**, 120 (1998).

[16] T. Fujisawa, D. G. Austing, Y. Tokura, Y. Hirayama, and S. Tarucha, *Allowed and Forbidden Transitions in Artificial Hydrogen and Helium Atoms*, Nature **419**, 278 (2002).

[17] J. M. Elzerman, R. Hanson, L. H. Willems van Beveren, L. M. K. Vandersypen, and L. P. Kouwenhoven, *Excited State Spectroscopy on a Nearly Closed Quantum Dot Via Charge Detection*, App. Phys. Lett. **84**, 4617 (2004).

[18] A. C. Johnson, J. R. Petta, J. M. Taylor, A. Yacoby, M. D. Lukin, C. M. Marcus, M. P. Hanson, and A. C. Gossard, *Tripletsinglet spin relaxation via nuclei in a double quantum dot*, Nature **435**, 925 (2005).

[19] G. Binnig, H. Roher, Ch. Gerber, and E. Weibel, *Surface studies by scanning tunneling microscopy*, Phys. Rev. Lett. **49**, 57 (1982).

[20] G. Binnig, C. F. Quate, and Ch. Gerber, *Atomic force microscope*, Phys. Rev. Lett. **56**, 930 (1986).

[21] M. A. Topinka, R. M. Westervelt, and E. J. Heller, *Imaging Electron Flow*, Phys. Today **Dec**, 47 (2003).

[22] M. A. Topinka, B. J. LeRoy, R. M. Westervelt, S. E. J. Shaw, R. Fleischmann, E. J. Heller, K. D. Maranowski, and A. C. Gossard, *Imaging Coherent Electron Flow From a Quantum Point Contact*, Science **289**, 2323 (2000).

[23] M. A. Topinka, B. J. LeRoy, R. M. Westervelt, S. E. J. Shaw, R. Fleischmann, E. J. Heller, K. D. Maranowski, and A. C. Gossard, *Coherent Branched Flow in a Two-Dimensional Electron Gas*, Nature **410**, 183 (2001).

[24] G. Finkelstein, P. I. Glicofridis, R. C. Ashoori, and M. Shayegan, *Topographic Mapping of the Quantum Hall Liquid Using a Few-Electron Bubble*, Science **289**, 90 (2000).

[25] A. Yacoby, H. F. Hess, T. A. Fulton, L. N. Pfeiffer, and K. W. West, *Electrical imaging of the quantum Hall state*, Solid State Comm. **111**, 1 (1999).

[26] N. B. Zhitenev, T. A. Fulton, A. Yacoby, H. F. Hess, L. N. Pfeiffer, and K. W. West, *Imaging of localized electronic states in the quantum Hall regime*, Nature **404**, 473 (2000).

[27] E. Ahlswede, P. Weitz, J. Weis, K. von Klitzing, and K. Eberl, *Hall potential profiles in the quantum Hall regime measured by a scanning force microscope*, Physica B **298**, 562 (2001).

[28] T. Ihn, J. Rychen, T. Vancura, K. Ensslin, W. Wegscheider, and M. Bichler, *Local Spectroscopy of Edge Channels in the Quantum Hall Regime with Local Probe Techniques*, Physica E **13**, 671 (2002).

[29] M. A. Topinka, *Imaging Coherent Electron Flow Through 2-D Electron Gas Nanostructures*, PhD Thesis, Harvard University (2002).

[30] B. J. LeRoy, *Imaging Coherent Electron Flow Through Semiconductor Nanostructures*, PhD Thesis, Harvard University (2003).

[31] I. H. Chan, *Quantum Dot Circuits: Single-Electron Switch and Few-Electron Quantum Dots*, PhD Thesis, Harvard University (2003).

[32] R. Crook, A. C. Graham, C. G. Smith, I. Farrer, H. E. Beere, and D. A. Ritchie, *Erasable electrostatic lithography for quantum components*, Nature **424**, 751 (2003).

[33] M. T. Woodside and P. L. McEuen, *Scanned Probe Imaging of Single-Electron Charge States in Nanotube Quantum Dots*, Science **296**, 1098 (2002).

[34] D. Rugar, R. Budakian, H. J. Mamin, and B. W. Chui, *Single spin detection by magnetic resonance force microscopy*, Nature **430**, 329 (2004).

[35] A. J. Heinrich, C. P. Lutz, J. A. Gupta, and D. M. Eigler, *Molecule Cascades*, Science **298**, 1381 (2002).

[36] P. Fallahi, A. C. Bleszynski, R. M. Westervelt, J. Huang, J. D. Walls, E. J. Heller, M. Hanson, and A. C. Gossard, *Imaging Electrons in a Single-Electron Quantum Dot*, AIP conf. Proc. **772**, 779 (2005).

[37] H. C. Manoharan, C. P. Lutz, and D. M. Eigler, *Quantum Mirages formed by Coherent Projection of Electronic Structure*, Nature **403**, 512 (2000).

[38] S. G. Lemay, J. W. Janssen, M. van den Hout, M. Mooij, M. J. Bronikowski, P. A. Willis, R. E. Smalley, L. P. Kouwenhoven, and C. Dekker, *Two-dimensional imaging of electronic wavefunctions in carbon nanotubes*, Nature **412**, 617 (2001).

[39] E. E. Vdovin, A. Levin, A. Patane, L. Eaves, P. C. Main, Yu. N. Khanin, Yu. V. Dubrovskii, M. Henini, and G. Hill, *Imaging the Electron Wave Function in Self-Assembled Quantum Dots*, Science **290**, 122 (2000).

[40] M. Mendoza and P. A. Schulz, *Wave-function mapping conditions in open quantum dot structures*, Phys. Rev. B **68**, 205302 (2003).

[41] A. Nogueira and A. Latge, *Mapping the electronic wave functions by determining current-voltage curves*, Phys. Rev. B **57**, 1649 (1998).

[42] J. Y. Marzin and J. M. Gerard, *Experimental Probing of Quantum-Well Eigenstates*, Phys. Rev. Lett. **62**, 127 (1989).

[43] G. Salis, B. Graf, K. Ensslin, K. Campman, K. Maranowski, and A. C. Gossard, *Wave Function Spectroscopy in Quantum Wells with Tunable Electron Density*, Phys. Rev. Lett. **79**, 5106 (1997).

[44] W. H. Press, B. P. Flannery, S. A. Teukolski, and W. T. Vetterling, *Numerical Recipes*, Cambridge University Press, 1986.

[45] A. Vidan, R. M. Westervelt, M. Stopa, M. Hanson, and A. C. Gossard, *Triple Quantum Dot Charging Rectifier*, Appl. Phys. Lett. **85**, 3602 (2004).

[46] K. E. Aidala, R. E. Parrott, T. Kramer, E. J. Heller, R. M. Westervelt, M. P. Hanson, and A. C. Gossard, *Imaging magnetic focusing of coherent electron waves*, in preparation (2006).

[47] P. Fallahi, A. C. Bleszynski, R. M. Westervelt, J. Huang, J. D. Walls, E. J. Heller, M. Hanson, and A. C. Gossard, *Imaging a Single-Electron Quantum Dot*, Nano Lett. **5**, 223 (2005).

[48] B. Schuh, *Algebraic Solution of a Non-Trivial Oscillator Problem*, J. Phys. A: Math. Gen. **18**, 803 (1985).